particles

MDPI

Article

Masses of Compact (Neutron) Stars with Distinguished Cores

Rico Zöllner [1,*], Minghui Ding [2] and Burkhard Kämpfer [2,3]

[1] Institut für Technische Logistik und Arbeitssysteme, TU Dresden, 01062 Dresden, Germany
[2] Helmholtz-Zentrum Dresden-Rossendorf, 01314 Dresden, Germany
[3] Institut für Theoretische Physik, TU Dresden, 01062 Dresden, Germany
* Correspondence: rico.zoellner@tu-dresden.de

Abstract: In this paper, the impact of core mass on the compact/neutron-star mass-radius relation is studied. Besides the mass, the core is parameterized by its radius and surface pressure, which supports the outside one-component Standard Model (SM) matter. The core may accommodate SM matter with unspecified (or poorly known) equation-of-state or several components, e.g., consisting of admixtures of Dark Matter and/or Mirror World matter etc. beyond the SM. Thus, the admissible range of masses and radii of compact stars can be considerably extended.

Keywords: compact stars; core-corona decomposition; impact of core mass; Dark-Matter admixture

check for updates

Citation: Zöllner, R.; Ding, M.; Kämpfer, B. Masses of Compact (Neutron) stars with Distinguished Cores. *Particles* **2023**, *6*, 217–238. https://doi.org/10.3390/particles6010012

Academic Editor: Armen Sedrakian

Received: 17 December 2022
Revised: 30 January 2023
Accepted: 31 January 2023
Published: 2 February 2023

1. Introduction

Strong interaction rules a variety of systems, ranging from hadrons to nuclei up to neutron stars. The related mass scales are typically $\geq m_\pi = 0.13\,\mathrm{GeV}$ for mesons, $\geq m_p = 0.938\,\mathrm{GeV}$ for baryons, $(1 \cdots 250)m_p$ for nuclei, and $\mathcal{O}(10^{57})m_p$ for neutron stars. ($m_{\pi,p}$ stand for pion and proton masses.) Further systems awaiting their confirmation are glueballs ($\mathcal{O}(\mathrm{GeV})$) and non-baryon stars, such as pion stars [1]. Besides weak interaction, it is the long-range Coulomb interaction that limits the size (or baryon number) of nuclei, and gravity is the binding force of matter in neutron stars. The phenomenon of hadron mass emergence is a fundamental issue tightly related to non-perturbative effects in the realm of QCD, cf., Refs. [2,3] and citations therein. Once the masses and interactions among hadrons are understood, one can make the journey to address the masses and binding energies of nuclei and then jump to constituents of neutron stars. Despite the notion, cool neutron stars accommodate, in the crust, various nuclei immersed in a degenerate electron-muon environment (maybe as "pasta" or "spaghetti" or crystalline medium). In the deeper interior, above the neutron drip density, neutrons and light clusters begin to dominate the matter composition. These constituents and their interactions govern the mass (or energy density) of the medium. At nuclear saturation density, $n_0 \approx 0.15\,\mathrm{fm}^{-3}$, one meets conditions similar to the interior of heavy nuclei but with crucial impact of the symmetry energy when extrapolating from nuclear matter with comparable proton and neutron numbers to a very asymmetric proton-neutron mixture. Above saturation density, various effects hamper a reliable computation of properties of the strong-interaction medium: three-body interactions may become even more important than at n_0, and further baryon species become excited, e.g., strangeness is lifted from vacuum into baryons forming hyperons whose interaction could be a miracle w.r.t. the hyperon puzzle [4], and the relevant degrees of freedom become relativistic. Eventually, at asymptotically high density, the strong-interaction medium is converted into quarks and gluons; color-flavor locking and color superconductivity can essentially determine the medium's properties. The turn of massive hadronic degrees of freedom into quark-gluon excitations is thereby particularly challenging.

While lattice QCD represents, in principle, an *ab initio* approach to strong-interaction systems in all their facets, the "sign problem" prevents the access to non-zero baryon

number systems. Thus, the exploration of compact/neutron stars, in particular their possible mass range, by stand-alone theory is presently not feasible. Instead, an intimate connection of astrophysical data and compact-star modeling is required.

The advent of detecting gravitational waves from merging neutron stars, the related multimessenger astrophysics [5–12] and the improving mass-radius determinations of neutron stars, in particular by NICER data [13–17], stimulated a wealth of activities. Besides masses and radii, moments of inertia and tidal deformabilities become experimentally accessible and can be confronted with theoretical models [18–24]. The baseline of the latter ones is provided by non-rotating, spherically symmetric cold dense matter configurations. The sequence of white dwarfs (first island of stability) and neutron stars (second island of stability) and possibly [25] a third island of stability [26–30] shows up when going to more compact objects, with details depending sensitively on the actual equation of state (EoS). The quest for a fourth island has been addressed as well [31,32]. "Stability" means here the damping of radial disturbances, at least. Since the radii of configurations of the second (neutron stars) and third (hypothetical quark/hybrid stars [33–40]) islands are very similar, the notion of twin stars [31–33,41,42] has been coined for equal-mass configurations; "masquerade" was another related term [43].

We emphasize the relation of ultra-relativistic heavy-ion collision physics, probing the EoS $p(T, \mu_B \approx 0)$, and compact star physics, probing $p(T \approx 0, \mu_B)$ when focusing on static compact-star properties [44,45]. Of course, in binary or ternary compact-star merging-events, also finite temperatures T and a large range of baryon-chemical potential μ_B are probed, which are accessible in medium-energy heavy-ion collisions [46]. Implications of the conjecture of a first-order phase transition at small temperatures and large baryo-chemical potentials or densities [47–50] can also be studied by neutron-hybrid-quark stars [51–54]. It is known since some time [26–28,55,56] that a cold EoS with special pressure-energy density relation $p(e)$, e.g., a strong local softening up to first-order phase transition with a density jump, can give rise to a "third family" of compact stars, beyond white dwarfs and neutron stars. In special cases, the third-family stars appear as twins of neutron stars [43,57,58]. Various scenarios of the transition dynamics to the denser configuration as mini-supernova have also been discussed quite early [59,60].

While the Standard Model (SM) of particle physics seems to accommodate nearly all of the observed phenomena of the micro-world, severe issues remain. Among them is the $(g-2)_\mu$ puzzle or the proton's charge radius. Another fundamental problem is the very nature of Dark Matter (DM): Astrophysical and cosmological observations seem to require inevitably its existence, but details remain elusive despite many concerted attempts, e.g., Refs. [61–64]. Supposing that DM behaves like massive particles, it could be captured gravitationally in the centers of compact stars [65–67], thus providing a non-SM component there. This would be an uncertainty on top of the less reliably known SM-matter state. Beyond the SM, other feebly interacting particles could also populate compact stars. A candidate scenario is provided, for instance, by Mirror World (MW) [68–72], i.e., a parity-symmetric complement to our SM-world with very tiny non-gravity interaction. There are many proposals of portals from our SM-world to such beyond-SM scenarios, cf., Ref. [73].

Guided by these remarks we follow here an access to static cold compact stars already launched in [74]: We describe the core by a minimum of parameters and determine the resulting compact-star masses and radii by assuming the knowledge of the equation of state of the SM-matter enveloping the core. A motivation is the quest of a mass gap between compact stars and black holes.

Our paper is organized as follows. In Section 2 we recall the Tolman–Oppenheimer–Volkoff equations, their scaling property, and introduce our core-corona decomposition. Small cores with and without MW/DM admixtures are considered in Section 3. Section 4 is devoted to the core-corona decomposition, where a specific EoS is deployed for the explicit construction. We summarize in Section 5. We supplement our paper in Appendix A by a brief retreat to the emergence of hadron masses as a key issue in understanding the typical scales of compact (neutron) star masses. Appendix B sketches a complementary approach:

the construction of an EoS by holographic means, thus transporting information of a hot (quark-gluon) QCD EoS to a cool EoS and connecting heavy-ion collisions and compact star physics. These appendices survey (Appendix A) and exemplify (Appendix B) symmetry and the governing principles where the access to astrophysical objects is based upon.

2. One-Component Static Cool Compact Stars: TOV Equations

The standard modeling of compact star configurations is based on the Tolman–Oppenheimer–Volkoff (TOV) equations

$$\frac{\mathrm{d}p}{\mathrm{d}r} = -G_N \frac{[e(r)+p(r)][m(r)+4\pi r^3 p(r)]}{r^2[1-\frac{2G_N m(r)}{r}]}, \tag{1}$$

$$\frac{\mathrm{d}m}{\mathrm{d}r} = 4\pi r^2 e(r), \tag{2}$$

resulting from the energy-momentum tensor of a one-component static isotropic fluid (described locally by pressure p and energy density e as only quantities relevant for the medium) and spherical symmetry of both space-time and matter, within the framework of Einstein gravity without cosmological term [75]. Newton's constant is denoted by G_N, and natural units with $c = 1$ are used, unless when relating mass and length and energy density, where $\hbar c$ is needed.

2.1. Scaling of TOV Equations and Compact/Neutron Star Masses and Radii

The TOV equations become free of any dimension by the scalings

$$e = \mathfrak{s}\bar{e}, \quad p = \mathfrak{s}\bar{p}, \quad r = (G_N\mathfrak{s})^{-1/2}\bar{r}, \quad m = (G_N^3\mathfrak{s})^{-1/2}\bar{m}, \tag{3}$$

where $\mathfrak{s}$ is a mass dimension-four quantity or has dimension of energy density. It may be a critical pressure of a phase transition or a limiting energy density, e.g., at the boundary matter-vacuum [76]. Splitting up $\mathfrak{s} = nm_p$ into a number density n and the energy scale m_p, one gets $(G_N\mathfrak{s})^{-1/2} = 7\ \mathrm{km}/\sqrt{10^{-2}n/n_0}$ and $(G_N^3\mathfrak{s})^{-1/2} = 4.8M_\odot/\sqrt{10^{-2}n/n_0}$, where the nuclear saturation density $n_0 = 0.15\ \mathrm{fm}^{-3}$ is used as reference density. The scales $m_{\pi,p}$ facilitate the densities $n = m_\pi^3 \to 2.3n_0$ and $n = m_p^3 \to 833n_0$. That is, the scale solely set by the nucleon mass, i.e., $\mathfrak{s} = m_p^4$ [77], yields $(G_N\mathfrak{s})^{-1/2} = 2.74$ km and $(G_N^3\mathfrak{s})^{-1/2} = 1.86M_\odot$, suggesting that the nucleon mass (see Appendix A on its emergence in QCD) determines the gross properties of neutron stars, such as mass and radius (modulus factor 2π) in an order-of magnitude estimate. In contrast, the density estimate via $M = \frac{4\pi}{3}\langle n\rangle m_p R^3$ yields, independently of G_N, $\langle n\rangle = 2n_0\frac{M}{M_\odot}\frac{10^3}{(R/\mathrm{km})^3} \approx 4n_0$ for $M = 2M_\odot$ and $R = 10$ km, thus pointing to the importance of the actual numerical values of $\bar{r}$ and $\bar{m}$.

In fact, recent measurements and supplementary work report averaged mean and individual heavy compact/neutron stars masses and radii (often on 67% credible level) as follows

PSR	$M\ [M_\odot]$	R **[km]**
	1.4	$11.94^{+0.76}_{-0.87}$ (1) [12], 12.45 ± 0.65 [13], $12.33^{+0.76}_{-0.81}$ [15]
J0030+0451	$1.34^{+0.15}_{-0.16}$	$12.71^{+1.14}_{-1.19}$ [16]
	$1.44^{+0.15}_{-0.14}$	$13.02^{+1.24}_{-1.06}$ [14], $12.18^{+0.56}_{-0.79}$ [17]
J1614–2230	1.908 ± 0.016 [78]	
J0348+0432	2.01 ± 0.04 [79]	
J0740+6620	$2.072^{+0.067}_{-0.066}$	$12.39^{+1.30}_{-0.98}$ [15]
	2.08 ± 0.07 [80]	$13.7^{+2.6}_{-1.5}$ (2) [13], $11.96^{+0.86}_{-0.81}$ [12]
0952-0607 (3)	2.35 ± 0.17 [81]	

(1) 90% confidence. (2) With nuclear physics constraints at low density and gravitational radiation data from GW170817 added in, the inferred radius drops to (12.35 ± 0.75) km [13]. (3) Black-widow binary pulsar PSR 0952-0607.

One has to add GW190814: gravitational waves from the coalescence of a 23 solar mass black hole with a $2.6M_\odot$ compact object [82]. An intriguing question concerns a possible mass gap between compact-star maximum-mass [83] and light black holes, cf., [84,85].

2.2. Solving TOV Equations

Given a unique relationship of pressure p and energy density e as EoS $e(p)$, in particular at zero temperature, the TOV equations are integrated customarily with boundary conditions $p(r=0)=p_c$ and $m(r=0)=0$ (implying $p(r)=p_c-\mathcal{O}(r^2)$ and $m(r)=0+\mathcal{O}(r^3)$ at small radii r), and $p(R)=0$ and $m(R)=M$ with R as circumferential radius and M as gravitational mass (acting as parameter in the external (vacuum) Schwarzschild solution at $r>R$). The quantity p_c is the central pressure. The solutions $R(p_c)$ and $M(p_c)$ provide the mass-radius relation $M(R)$ in parametric form.

A great deal of effort is presently concerned about the EoS at supra-nuclear densities [86]. For instance, Figure. 1 in Ref. [87] exhibits the currently admitted uncertainty: up to a factor of 10 in pressure as a function of energy density. At asymptotically large energy density, perturbative QCD constrains the EoS, though it is just the non-asymptotic supra-nuclear density region that crucially determines the maximum mass and whether twin stars may exist or quark-matter cores appear in neutron stars. Accordingly, one can fill this gap by a big number (e.g., millions [88]) of test EoSs to scan through the possibly resulting manifold of mass-radius curves, see Refs. [89–92]. However, the possibility that neutron stars may accommodate other components than Standard Model matter, e.g., exotic material as Dark Matter [93–96], can be an obstacle for the safe theoretical modeling of a concise mass-radius relation in such a manner. Of course, inverting the posed problem with sufficiently precise data of masses and radii as input offers a promising avenue towards determining the EoS [17,89,97–101].

Here, we pursue another perspective. We parameterize the supra-nuclear core by a radius r_x and the included mass m_x and integrate the above TOV equations only within the corona (our notion "corona" is a synonym for "mantel" or "crust" or "envelope" or "shell", it refers to the complete part of the compact star outside the core, $r_x \leq r \leq R$), i.e., from pressure p_x to the surface, where $p=0$. This yields the total mass $M(r_x, m_x; p_x)$ and the total radius $R(r_x, m_x; p_x)$ by assuming that the corona EoS $e(p)$ is reliably known at $p \leq p_x$ and that only SM matter occupies that region. Clearly, without knowledge of the matter composition at $p > p_x$ (may it be SM matter with an uncertainly known EoS or may it contain a Dark-Matter admixture, for instance, or monopoles or some other type of "exotic" matter) one does not get a simple mass-radius relation by such a procedure, but admissible area(s) over the mass-radius plane, depending on the core parameters r_x and m_x and the matching pressure p_x and related energy density e_x. This is the price of avoiding a special model of the core matter composition.

If the core is occupied by a one-component SM medium, the region $p > p_x$ and $e > e_x$ can be mapped out by many test EoSs which locally obey the constraint $v_s^2 \in [0,1]$ to obtain the corresponding region in the mass-radius plane, cf., Figure 2 in Ref. [102] for an example processed by Bayesian inference. This is equivalent, to some extent, to our core-corona decomposition for SM matter-only.

3. Small-Core Approximation and Beyond

3.1. One-Component Core

For small one-component distinguished cores one can utilize the EoS parameterization from a truncated Taylor expansion of $p(e) \geq p_x$ at λe_x, $p(e) = p(\lambda e_x) + \frac{\partial p}{\partial e}|_{\lambda e_x}(e-\lambda e_x) + \cdots$,

$$p(e) = p_x + v_s^2(e - \lambda e_x), \tag{4}$$

where $\lambda > 1$ is a density jump at the core boundary and $\lambda = 1$ continuously continues (but may be kinky) the corona EoS at $p \geq p_x$; p_x and e_x mark the "end point" of the corona EoS. A Taylor expansion for small cores,

$$p(r) = \sum_{i=0}^{\infty} p_{2i} r^{2i}, \tag{5}$$

$$m(r) = \sum_{i=0}^{\infty} m_{2i+1} r^{2i+1}, \tag{6}$$

gives by means of Equations (1) and (2) with (4) (that is $e = \lambda e_x - v_s^{-2} p_x + v_s^{-2} \sum_{i=0}^{\infty} p_{2i} r^{2i}$) and $p_{2i+1} = 0$ and $m_{2i} = 0$ for all $i \in \mathbb{N}_0$

$$m_1 = 0,\ m_3 = \frac{4\pi}{3} e_c,\ m_{2i+1} = \frac{4\pi v_s^{-2}}{2i+1} p_{2i-2} \text{ for } i \geq 2, \tag{7}$$

where $e_c \equiv e(p_c) = \lambda e_x + v_s^{-2}(p_c - p_x)$, and the recurrence

$$p_0 = p_c, \quad p_2 = -\frac{2\pi}{3} G_N (e_c + p_c)(e_c + 3p_c), \tag{8}$$

$$p_{2i} = \frac{G_N}{2i} \Big(2A_i - [\lambda e_x - v_s^{-2} p_x](m_{2i+1} + 4\pi p_{2i-2}) - (1 + v_s^{-2}) B_{i-1} \Big) \text{ for } i \geq 1, \tag{9}$$

$$A_i = \sum_{j=0}^{i} 2(i-j) m_{2j}\, p_{2i-2j}, \tag{9'}$$

$$B_i = \sum_{j=0}^{i} (m_{2j+3} + 4\pi p_{2j})\, p_{2i-2j}. \tag{9''}$$

In leading order one obtains

$$r_x \approx \frac{\delta^{1/2}(1 - \mathcal{O}(\delta))}{\sqrt{\frac{2\pi}{3} G_N p_x W}} \approx \frac{60.1 \text{ km}}{\sqrt{W}} \sqrt{\delta \frac{100 \text{ MeV/fm}^3}{p_x}}, \tag{10}$$

$$m_x \approx 2\lambda \frac{e_x}{p_x} \frac{\delta^{3/2}(1 - \mathcal{O}(\delta))}{\sqrt{\frac{2\pi}{3} G_N^3 p_x W^3}} \approx \frac{81.2 M_\odot}{W^{3/2}} \lambda \frac{e_x}{100 \text{ MeV/fm}^3} \times \left(\delta \frac{100 \text{ MeV/fm}^3}{p_x} \right)^{3/2}, \tag{11}$$

where $\delta := p_c/p_x - 1$ and $W := 3 + 4\lambda \frac{e_x}{p_x} + \lambda^2 \left(\frac{e_x}{p_x} \right)^2$. The scale setting is by p_x and $\lambda e_x / p_x$. The core-mass–core-radius relation is $m_x(\delta) \approx \frac{4\pi}{3} p_x \lambda \left(\frac{e_x}{p_x} \right) r_x(\delta)^3 (1 + \mathcal{O}(\delta))$.

To control and extend the above approximations we numerically solve the scaled TOV equations by assuming that Equation (4) holds true in the core. (Of course, this is an *ad hoc* assumption aimed at providing an explicit example of mass-radius relations of the core.) The core-corona matching is at p_x, i.e., the maximum (minimum) pressure of the corona (core) EoS. The related energy density is $e_x = 3p_x/(1 - 3\Delta^{corona})$, where Δ^{corona} denotes the trace anomaly measure discussed below in Equation (12). It is used here for a suitable parameterization of the double (e_x, p_x) by means of the corona EoS. The core EoS Equation (4), $e(p) = \lambda e_x + v_s^{-2}(p - p_x)$, enters, after scaling according to Equation (3), the dimensionless TOV equations

$$\frac{\mathrm{d}\bar{p}}{\mathrm{d}\bar{r}} = -\frac{[\bar{e}(\bar{r}) + \bar{p}(\bar{r})][\bar{m}(\bar{r}) + 4\pi \bar{r}^3 \bar{p}(\bar{r})]}{\bar{r}^2 [1 - \frac{2\bar{m}(\bar{r})}{\bar{r}}]}, \tag{1'}$$

$$\frac{\mathrm{d}\bar{m}}{\mathrm{d}\bar{r}} = 4\pi \bar{r}^2 \bar{e}(\bar{r}), \tag{2'}$$

for $\bar{p} \in [\bar{p}_c, \bar{p}_x]$ to get $\bar{r}_x(\bar{p}_c)$ and $\bar{m}_x(\bar{p}_c)$. The corresponding scaled core mass vs. core radius relations are exhibited in Figure 1, where the scaling quantity $\mathfrak{s} = p_x$ is employed, i.e., $\bar{p}_x = 1$. The figure offers a glimpse on the systematic of the parameter dependence. Note that it applies to all values of $p_x > 0$. The finite pressure and energy density at the core boundary facilitates a pattern of mass-relations and dependence on sound velocity as known from bag model EoS, cf., Figure 7 in Ref. [76]. $\lambda > 1$ causes an overall shrinking of the pattern plus a slight up-shift; see the right panel for $\lambda = 1.5$. Considering, e.g., $e_x \in [150, 1500]$ MeV/fm^3 and the scaling $\propto 1/\sqrt{e_x}$, cf., (3), the core masses and radii change by a factor up to three, depending on the actual value of e_x.

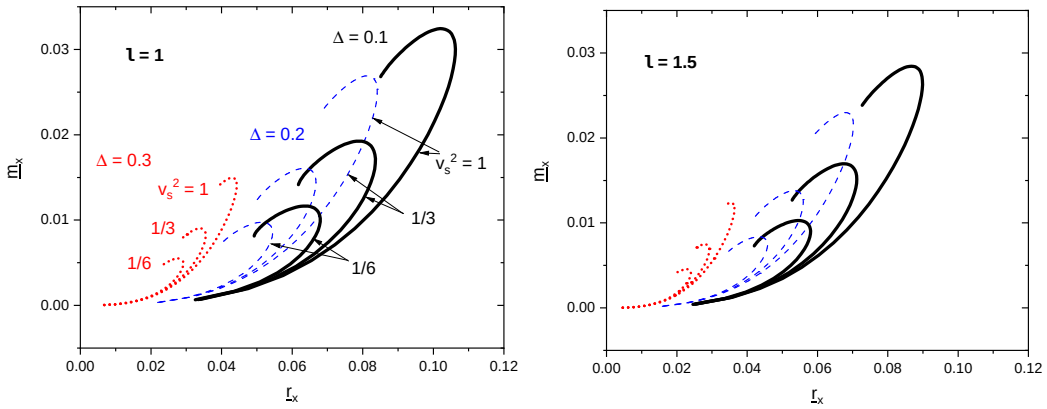

Figure 1. Scaled core masses $\bar{m}_x$ as a function of the scaled core radii $\bar{r}_x$ for various values of $\Delta^{corona} = \Delta$ and v_s^2 for a one-component medium with EoS (4). The **left** (**right**) panel is for $\lambda = 1$ (1.5). The scaling quantity is $\mathfrak{s} = p_x$. For central pressures $\bar{p}_c = 1.1^n$, $n = 1 \cdots 55$. The displayed curves are limited by $\bar{m}_x < \bar{r}_x/2$ (black hole limit) and $\bar{m}_x > \frac{4\pi}{3}\lambda\frac{3}{1-3\Delta^{corona}}\bar{r}_x^3$. The latter expression is for the respective asymptotic curve in the small-$\bar{r}_x$ region. To convert to usual dimensions, one employs $r_x = \bar{r}_x \frac{86.9 \text{ km}}{\sqrt{p_x/100 \text{ [MeV/fm}^3\text{]}}}$ and $m_x = \bar{m}_x \frac{58.8\ M_\odot}{\sqrt{p_x/100 \text{ [MeV/fm}^3\text{]}}}$, where "$p_x/100$ [MeV/fm^3]" denotes the scaling pressure p_x in units of 100 MeV/fm^3. The approximations (10) and (11) apply only in the small-$\bar{m}_x$ and small-$\bar{r}_x$ regions.

3.2. Multi-Component Cores

In a multi-component medium (note that our considerations apply to components which do not mutually interact in a direct microscopical manner, but are coupled solely by the common gravity field) with known EoSs one has to add the contributions by $[m(r) + 4\pi r^3 p(r)] \to \sum_i [m_{(i)}(r) + 4\pi r^3 p_{(i)}(r)]$ and $[1 - \frac{2G_N m(r)}{r}] \to [1 - \frac{2G_N \sum_i m_{(i)}(r)}{r}]$ and solve in parallel the multitude of TOV equations for the components i. A particular minimum-parameter model is Mirror World matter (component $i = 2$) which is completely symmetric to SM matter (component $i = 1$), i.e., $p_{(1)}(r) = p_{(2)}(r)$ etc., turning $\sum_{(i)} \to 2$. The results are exhibited in Figure 2, left. The increased energy density by the two superimposed fluids cause a shrinking of the core-mass–core-radius curves similar to the increase of λ in Figure 1. The extension to three components is exhibited in Figure 2, right. Here, $\sum_{(i)} \to 3$ applies. Due to further increased energy density and pressure, the configurations become even more "compact", i.e., core masses and core radii shrink further on.

One may quantify the core compactness by $\bar{\mathcal{C}}_x := 2\bar{m}_x^{max}/\bar{r}_x|_{\bar{m}_x^{max}}$ and note that, within the scanned parameter patch, it (i) is independent of the number of fluids, (ii) increases slightly with Δ^{corona} at $v_s^2 = const$ and (iii) decreases with decreasing $v_s^2 = const$ at $\Delta^{corona} = const$, see Table 1. Note that the usual definition of compactness is without the factor of two.

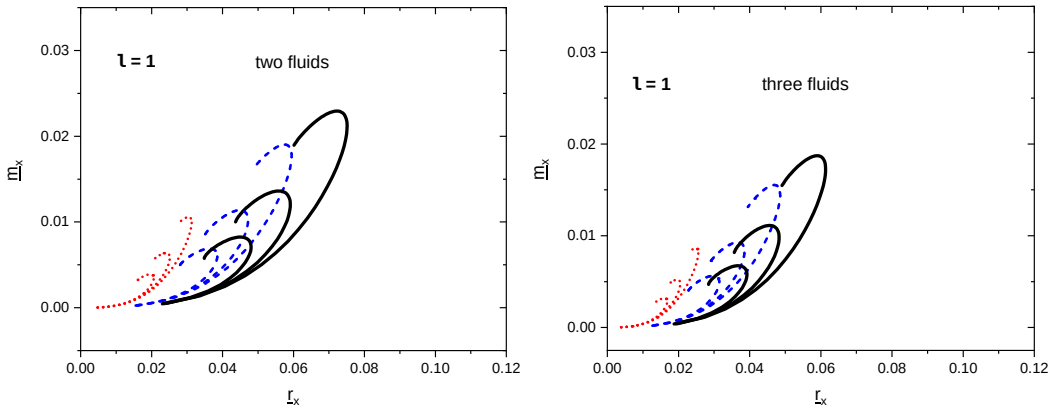

Figure 2. Left panel: As the left panel of Figure 1, but for a two-component medium of SM + MW matter with $p_{(1)}(r) = p_{(2)}(r)$ and EoS (4) for both components. Note the difference to the two-fluid core-shell construction in Ref. [103]. **Right** panel: As a left panel but for a three-component medium.

Table 1. Core compactness $\bar{\mathcal{C}}_x = 2\bar{m}_x^{max}/\bar{r}_x|_{\bar{m}_x^{max}}$ for various values of v_s^2 (sound velocity squared in the core) and $\Delta^{corona} = \Delta$. For $\lambda = 1$.

v_s^2 \ Δ	**0.1**	**0.2**	**0.3**
1	0.64	0.67	0.70
1/3	0.49	0.51	0.53
1/6	0.37	0.38	0.40

Of course, more general is an asymmetric Mirror World component facilitating $p_{(1)}(r) \neq p_{(2)}(r)$, especially $p_{(1)}(r = 0) \neq p_{(2)}(r = 0)$, even for the common EoS (4), dealt with in Appendix A in Ref. [74]. We do not dive into various conceivable scenarios here and refer the interested reader to Refs. [103,104].

4. Core-Corona Decomposition with NYΔ DD-EM2 EoS

4.1. Trace Anomaly

An example of an EoS largely compatible with neutron star data is NYΔ based on the DD-ME2 density functional [31]. Despite some peculiarities (see the left panel in Figure 3), it shares features recently advocated as essential w.r.t. QCD tracy anomaly and conformality [105,106]. A suitable measure of the trace anomaly is

$$\Delta := \frac{1}{3} - \frac{p}{e} \tag{12}$$

which is related to the sound velocity squared

$$v_s^2 := \frac{\partial p}{\partial e} = \frac{n_B}{\mu_b \chi_B} = \frac{1}{3} - \Delta - e\frac{\partial \Delta}{\partial e}, \tag{13}$$

where n_B stands for the baryon density, μ_B the baryo-chemical potential, and $\chi_B = \partial^2 p/\partial \mu_B = \partial n_B/\partial \mu_B$ is the second-order cumulant of the net-baryon number density. Thermodynamic stability and causality constrain $\Delta \in [-2/3, 1/3]$. Restoration of scale invariance means $\Delta \to 0$ and $v_s^2 \to 1/3$. Although Δ approaches monotonically to zero, v_s^2 can develop a peak at lower energy densities. In fact, v_s^2 as a function of $\eta \equiv \ln e/(n_0 m_p)$ displays such a peak at $\eta \approx 1.3$ (see Figure 2 in Ref. [105] or Figure 1 in Ref. [88] and discussion in Ref. [107]), which should be considered a signature of conformality even at strong coupling. Continuing with the adjustment of Δ beyond the values tabulated in

Ref. [31] (see the symbols in Figure 3, left), v_s^2 drops first slightly below $1/3$ and approaches then slowly $1/3$ from below, in agreement with QCD asymptotic.

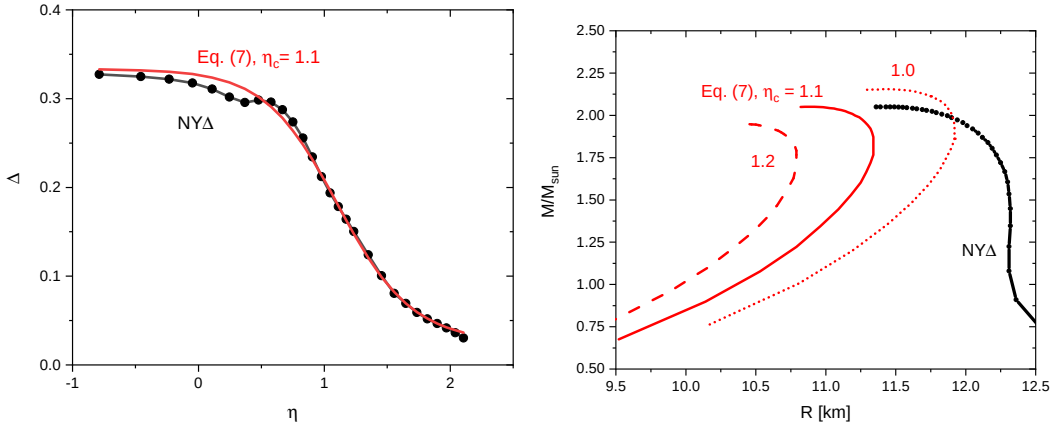

Figure 3. Left panel: Trace anomaly measure $\Delta = 1/3 - p/e$ as a function of $\eta \equiv \ln e/(n_0 m_p)$ for the NYΔ DD-EM2 EoS of [31] (black curve with symbols) and the adjusted parameterization by Equation (7) in Ref. [105] (red curve; $\eta_c = 1.1$, other parameters as in Ref. [105], see Equation (14) below). NYΔ DD-EM2 shows a softening at $p \approx 10$ MeV/fm^3, $\eta \approx 0.5$, caused by the onset of Δ proliferation, similar to Ref. [108]. **Right** panel: Mass-radius relation for NYΔ DD-EM2 EoS of Ref. [31] (solid black curve) in comparison with the parameterization by Equation (7) in Ref. [105] (see Equation (14) below for three values of the parameter η_c (read dashed/solid/dotted curves for $\eta_c = 1.2$, 1.1 and 1.0).

The comparison of the resulting mass-radius relations is exhibited in Figure 3, right. We follow the parameterization [105]

$$\Delta = \frac{1}{3} - \frac{1}{3}\left(1 - \frac{A}{B+\eta^2}\right)\frac{1}{1+e^{-\kappa(\eta-\eta_c)}}, \tag{14}$$

however, with parameters adjusted to [31]: $\kappa = 3.45$, $\eta_c = 1.1$, $A = 2$ and $B = 20$, see Figure 3. Despite the tiny differences of the red curve (for adjusted Δ) and the solid black curve with markers (for NYΔ DD-EM2 EoS of [31]), the overall shapes of $M(R)$ differ in detail, see Figure 3, right. While the maximum masses agree, the radii for NYΔ DD-EM2 EoS of [31] are greater by about 1 km at $M \approx 1.4\ M_\odot$. A small dropping of the parameter η_c from 1.2 to 1.0 in the Δ EoS lets us increase the radius by 1 km. All these differences can be traced back essentially to differences in the low-density part of the employed EoSs.

4.2. Distinguished Cores with NYΔ Envelope

Focusing now on NYΔ DD-EM2 EoS of Ref. [31] and the core-corona decomposition, one obtains the resulting mass-radius radius relation exhibited in Figure 4. We find it convenient to keep the respective core radius constant and vary the core masses as $m_x = 10^{-4}1.5^n M_\odot$, $n = 1, 2, 3\cdots$. The very small core masses (of course, a large core with several-km radius and small included mass is a very exotic thing; it may be referred to as bubble or void with surface pressure p_x and the stable interface to SM matter) occupy the right end of the solid blue curves, where the dots refer to the increasing values of n. Heavy core masses occupy the left sections of the blue curves, i.e., larger values of n. For considerably smaller values of the core radii (not displayed), the blue curves approach the conventional mass-radius curve of the NYΔ DD-EM2 EoS of Ref. [31] (fat black curve). The limit $r_x \to 0$ and $m_x \to 0$ of the core-corona decomposition curve is depicted by the asterisk, which also agrees with the mass and radius of NYΔ DD-EM2 EoS of Ref. [31] with $p_c = p_x$. Increasing values of p_x make an up-shift of the core-corona mass-radius curves for a constant value of the core radius r_x, and a larger range of masses is occupied.

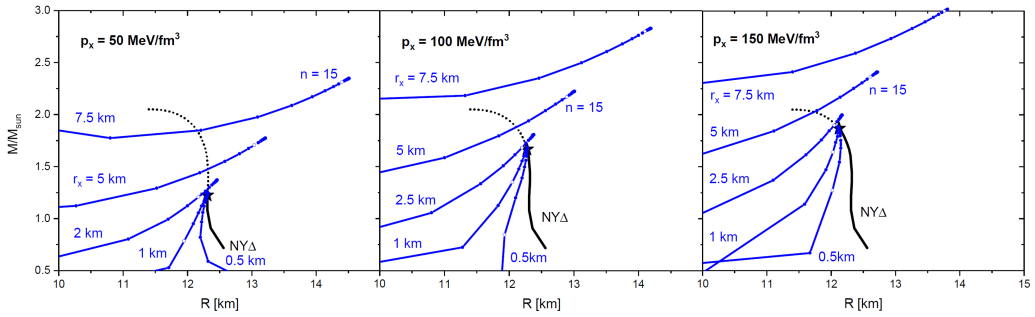

Figure 4. Mass-radius plane and its occupancy by compact stars with given core radii r_x (blue curves with dots at core masses $m_x = 10^{-4}\ 1.5^n M_\odot$, $n = 1, 2, 3 \cdots$ from right to left; the open circles depict points for $n = 15$, and the right-most endpoints are for $n = 1$). The values of p_x are 50 (**left** panel), 100 (**middle** panel), and 150 MeV/fm^3 (**right** panel). The fat solid curve is obtained by standard integration of the TOV equations using the NYΔ EoS tabulated in Ref. [31] with linear interpolation both in between the mesh and from the tabulated minimum energy density to the $p = 0$ point at $e_0 = 1$ MeV/fm^3. The asterisks display the mass-radius values for $p_c = p_x$. That is, the sections above the asterisks (dotted curves) are for a particular continuation of NYΔ at $p > p_x$, which is, (trivially) in this case, NYΔ itself. One could instead employ the parameterization Equation (4) which would deliver another dotted curve. For other examples, in particular the small-R region near black hole and Buchdahl limits, the interested reader is referred to Ref. [74].

All the features discussed in Section 2 in Ref. [74] are recovered, e.g., the convex shape of the curves $r_x = const$, which however becomes visible only by extending the plot towards smaller values of R (not shown). The right end points of the core-corona curves refer to very small values of m_x, while the not displayed left end points are on the limiting black hole curve $2G_N M = R$. However, the core-corona decomposition shows that the maximum-mass region of NYΔ-DD-ME2 (see fat solid curves) is easily uncovered too, interestingly with sizeable core radii and noticeably smaller up to larger total radii.

We refrain from displaying the core-corona mass-radius curves for $m_x = const$. They can be easily inferred by connecting the points $n = const$ in each of the panels in Figure 4.

To stress the relation to the usual mass-radius relation $M(R)$ obtained from the parametric representations $M(p_c)$ and $R(p_c)$, let us mention that the respective dotted curve sections above the asterisk on the fat solid curves are just an example—here simply NYΔ DD-EM2 EoS of Ref. [31] for $p > p_x$. Other continuations of the EoS at $p > p_x$ are within the region filled by the blue core-corona curves, which however may not be completely mapped out by many conceivable EoSs: The core can contain more than just SM matter, such as Dark Matter or Mirror Matter or other exotic material. In the simplest case, a multi-component composition with hypothesized EoS for each component can be used for the explicit construction. All that counts in our core-corona decomposition is that a core with radius r_x and included mass m_x is present and supports the pressure p_x at its boundary. By definition, outside the core, only SM matter with known EoS is there. (For a dedicated study of crust properties, cf., Ref. [109].)

4.3. Example of Radial Pressure and Mass Profiles

To illustrate that feature in some detail let us consider an example and select $p_x = 100$ MeV/fm^3. Assuming that the continuation of the EoS above this p_x is, hypothetically, by NYΔ itself, one obtains the pressure and mass profiles as displayed by black solid curves in Figure 5 for $p_c = 200$ MeV/fm^3. Clearly, taking r_x, m_x and p_x as start values and integrating in the corona up to the surface at $p = 0$, one obtains the same values of M and R as for the standard integration from $p(r = 0) = p_c$ to $p(R) = 0$ (see the blue circles on top of the black solid curve sections). However, keeping r_x but using other core masses m_x, e.g., $m_x^{(1)} = 0.5 m_x$ or $m_x^{(2)} = 2 m_x$, one obtains different pressure and mass profiles and, consequently, also different values of M and R, see Figure 5. This is the very construction of the core-corona decomposition leading to the results exhibited in Figure 4.

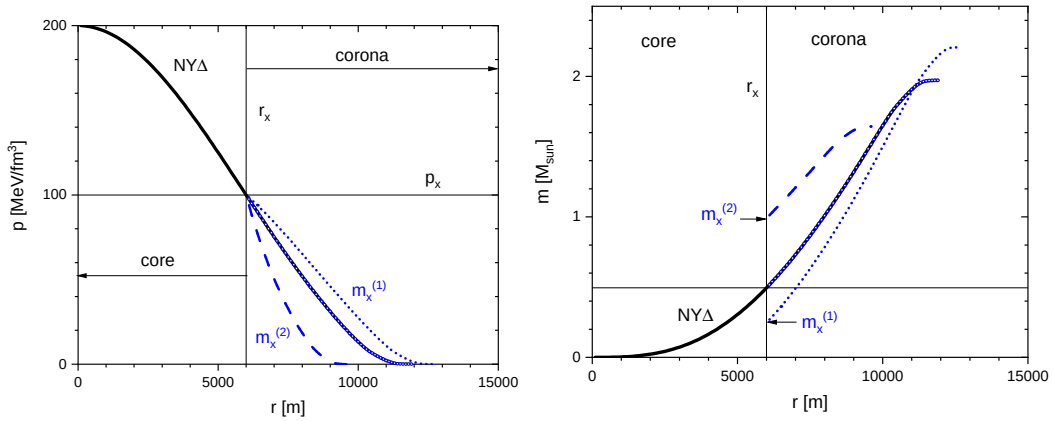

Figure 5. Pressure $p(r)$ (**left** panel) and mass $m(r)$ (**right** panel) as a function of the radius r for the special value $p_x = 100$ MeV/fm^3, selected here as the end point of the "reliable EoS" NYΔ at $p \leq p_x$. Assuming a possible continuation at $p > p_x$ by NYΔ itself as a particular example, it yields the fat solid curves for the (ad hoc) choice $p_c = 200$ MeV/fm^3. Keeping the resulting value r_x from $p(r_x) = p_x$ and integrating the TOV equations in the corona, $r \geq r_x$ with p_x and $m_x^{(1,2)}$ as initial values, one gets the dashed blue ($m_x^{(1)} = 0.5m_x$) and dotted blue ($m_x^{(2)} = 2m_x$) curves, where the respective values of R and M can be read off. Using m_x as core mass, the blue circles (on top of the fat black curve at $r \geq r_x$) are obtained. Using a multitude of values $m_x^{(n)}$ would generates one additional blue curve in Figure 4. In the present example, for $r_x = 6$ km.

5. Summary

The core-corona decomposition relies on the assumption that the EoS of compact/neutron star matter (i) is reliably known up to energy density e_x and pressure p_x and (ii) occupies the star as the only component at radii $r \geq r_x$. The base line for static, spherically symmetric configurations is then provided by the TOV equations, which are integrated, for $r \in [r_x, R]$, to find the circumferential radius R (where $p(R) = 0$) and the gravitational mass $M = m(R)$. We call that region $r \in [r_x, R]$ "corona", but "crust" or "mantle" or "envelope" or "shell" are also suitable synonyms. The region $r \in [0, r_x]$ is the "core", which is parameterized by the included mass m_x. The core must support the corona pressure at the interface, i.e., $p(r_x^-) = p(r_x^+)$. The core can contain any material compatible with the symmetry requirements. In particular, it could be modeled by a multi-component fluid with SM matter plus Dark Matter and/or Mirror World matter or anything beyond the SM. The TOV equations then deliver $R(r_x, m_x, p_x)$ and $M(r_x, m_x, p_x)$.

It helps our intuition to think of a SM matter material in the core with assumed fiducial EoS, which determines, for given value of p_x, $r_x(p_c)$ and $m_x(p_c)$, thus $R(p_c)$ and $M(p_c)$ resulting in $M(R)$, as conventionally done. Using many fiducial test EoSs at $p > p_x$, one maps out a certain region in the M-R plane accessible by SM matter. Our core-corona decomposition extends this region, since the core can contain much more than SM matter only. With reference to a special EoS, applied tentatively in core and corona, the accessible masses and radii become smaller (larger) for heavy (light) cores. That effect is noticeable for large (km size) and heavy (fraction of solar mass) cores. Small and light cores hardly have an impact.

This analysis should be refined in follow-up work by employing improved EoSs in the low-density region and by taking care of mass-radius values for the heaviest neutron star(s), still keeping precise radius values for the $1.4M_\odot$ neutron stars. In addition, the holographic model in Appendix B, which is aimed at mapping hot QCD thermodynamics to a cool EoS, deserves further investigations, before arriving quantitatively at an EoS suitable for compact star properties and (merging) dynamics. The emphasis in Appendix B is the illustration of the extrapolation scheme beyond a patch of QCD thermodynamic state space.

Taking up the suggestion in Ref. [77] that the scaling property of the TOV equations with a mass dimension-4 quantity, e.g., by m_p^4, where m_p is the proton mass, essentially determines the gross parameters of compact/neutron stars, we supply in Appendix A a brief contemplation on the emergence of hadron masses within QCD-related approaches, thus bridging from micro to macro physics: $M_{PSR\,J0740+6620} \approx 2M_\odot \approx 2.38 \times 10^{57} m_p$, $R_{PSR\,J0740+6620} \approx 12.3$ km $\approx 1.5 \times 10^{19} r_p$ with proton charge radius $r_p \approx 0.88$ fm $\approx 4.2 m_p^{-1}$ which is somewhat larger than its "natural" scale $\hbar c/m_p$. Our focus, however, is here on the emergence of the gravitational mass (the gravitational mass in our core-corona decomposition is $M = m_x + 4\pi \int_{r_x}^{R} \mathrm{d}r r^2 e(r)$ which, due to gravitational binding, is different from the total mass $\int \mathrm{d}^3 V e(r)$ where the integral measure $\mathrm{d}^3 V$ accounts for the gravitational spatial deformation, cf., Ref. [110]) determining the trajectories of light rays and test particles outside of compact astrophysical objects.

Author Contributions: Conceptualization, B.K.; methodology, R.Z., M.D., and B.K.; validation, R.Z., M.D. and B.K.; investigation, R.Z., M.D., and B.K.; writing—original draft preparation, B.K.; writing—review and editing, B.K. and R.Z.; visualization, B.K. and R.Z.; supervision, B.K.; project administration, B.K. All authors have read and agreed to the published version of the manuscript.

Funding: The work is supported in part by the European Union's Horizon 2020 research and innovation program STRONG-2020 under grant agreement No 824093.

Acknowledgments: We thank S. M. Schmidt and C. D. Roberts for inviting our contribution to the topic of the emergent mass phenomenon. M. Ding is grateful for support by Helmholtz-Zentrum Dresden-Rossendorf High Potential Programme. One of the authors (BK) acknowledges continuous discussions with J. Schaffner-Bielich and K. Redlich and for the encouragement to deal with the current topic.

Conflicts of Interest: The authors declare no conflict of interest.

Appendix A. Emergence of Hadron Masses

Astronomical observations of neutron stars have provided us with a way to understand these mysterious objects. The literature suggests that the outer and inner core of neutron stars may consist of nucleons or cold, dense quark matter. The question one can ask is how almost massless light quarks could combine and produce such massive nucleons to give rise to neutron star mass, as emphasized in Section 2.1. A widely recognized mechanism is the Higgs mechanism, which gives rise to the current quark masses. However, as was immediately realized, the current quark mass contributes only a few MeV, while the mass of a proton or neutron is much larger. The mystery of the missing masses lies in the emergence of hadron mass (EHM).

Appendix A.1. Three Pillars of EHM

Contemporary studies of continuum Schwinger methods (CSMs) have shown that the emergence of hadron mass rests on three pillars: (a) the running quark mass, (b) the running gluon mass, and (c) the process-independent effective charge. These three pillars provide the basis for giving observable results of hadron properties [111].

Appendix A.1.1. Running Quark Mass

The first pillar is the most familiar, namely the running quark mass. The dressed-quark propagator can be represented by a special quantity, the dressed-quark mass function. Modern CSMs calculations of the quark gap equation show that the dressed-quark mass function is a finite value of $M_0(k^2 = 0) = 0.41$ GeV in the far infrared, even in the chiral limit. This is an explicit expression of the dynamical chiral symmetry breaking (DCSB), and the infrared scale is responsible for the masses of all hadrons, and the running quark mass is therefore regarded as an expression of the EHM. In a sense, the quark in the far infrared can be seen as a quasiparticle, produced by the interaction of the high-energy quark parton with the gluon. The scale of the dressed-quark mass function in the far

infrared is comparable to the scale in the constituent quark model. The difference is that the dressed-quark mass function is momentum-dependent, and it runs from the far infrared to the ultraviolet, where it matches the current quark mass in perturbation theory. The dressed-quark mass function is also flavor-dependent, with the Higgs mechanism gradually dominating in describing it from light to heavy quarks, while the dressed-quark mass function decreases at a slower rate. It is worth emphasizing that the ultraviolet behavior of the dressed-quark mass function in the chiral limit is related to the well known chiral condensates.

Appendix A.1.2. Running Gluon Mass

The second pillar is the running gluon mass. Gauge invariance requires that the gluon parton be massless. However, in the Schwinger mechanism of QCD, it was conjectured long ago that the two-point gluon Schwinger function might give rise to a massive dressed gluon. Thus, the dressed gluon gains mass and the gluon parton is transformed into the gluon quasiparticle by interaction with themselves. Consequently, gluons can have a momentum-dependent mass function, and this non-zero function has been confirmed by both the continuum and lattice QCD. The dressed gluon mass function is power-law suppressed in the ultraviolet, so it is invisible in perturbation theory. However, it is non-zero in the infrared momentum range, and in the far infrared it yields a value of $m_g = 0.43$ GeV. This is purely a manifestation of "mass from nothing" and is responsible for all hadron masses. It is worth emphasizing that the running gluon mass may also be associated with confinement. The gluon two-point Schwinger function has an inflection point, so it has no Källén-Lehmann representation, and therefore the relevant states cannot appear in the Hilbert space of physical states.

Appendix A.1.3. Process-Independent Effective Charge

The third pillar is the process-independent effective charge. QCD has a running coupling which expresses the feature of asymptotic freedom in the ultraviolet at one-loop order, but it also shows a Landau pole in the infrared, where the coupling becomes divergent when $k^2 = \Lambda^2_{\rm QCD}$. However, recent advances in CSMs based on pinch techniques and background field methods show that QCD has a unique, nonperturbatively well-defined, computable, process-independent effective charge. Its large-momentum behavior is smoothly connected to the QCD running coupling at one-loop order, while it is convergent at small momentum. The Landau pole is eliminated due to the appearance of the gluon mass scale in the infrared. It is noteworthy that, at small momentum, the effective charge run ceases and it enters a domain that can be regarded as an effective conformal. In this domain, the gluons are screened so that the valence quasiparticle can be seen as carrying all the properties of a hadron. Furthermore, the process-independent effective charge matches the Bjorken process-dependent charge, and in practical use they can be considered to be indistinguishable. Additionally, the process-independent effective charge is a well-defined smoothing function at all available momenta, from the far infrared to the ultraviolet, so it can be a good candidate for applications, for example, in evolving parton distribution functions to different scales.

Appendix A.2. Hadrons in Vacuum

A direct correlation with the running quark mass is its effect on pseudoscalar mesons, especially the lightest meson, the pion [112,113]. As a chiral symmetry breaking Nambu–Goldstone boson, the well-known Goldberger–Treiman relation relates the dressed-quark mass function to pion's Bethe–Salpeter amplitude, so that, to some extent, it can be seen that, once the one-body problem is solved, the two-body problem is also solved. Furthermore, because of its direct connection to the dressed quark mass function, the properties of the pion can be seen as the cleanest window to glimpse the emergence of hadron mass. In the quark model, the vector meson is a spin-flip state of the pseudoscalar meson, and thus the ρ meson is the closest relative to pions. However, the properties of ρ mesons are

significantly different from those of pion. Compared to the surprisingly light pion, the ρ is much heavier. Therefore, one can ask a straightforward question: how does the spin flip produce such different masses for the two mesons? Since QCD is a well-defined theory of strong interactions, it must answer such a fundamental question.

The meson spectrum includes not only ground states, but also excited states with high orbital angular momenta between the quark and antiquark constituents of the meson. The study of excited mesons is more difficult in both lattice QCD and CSMs. Experience tells us that the well-known rainbow ladder approximation does not provide the correct ordering of the meson masses between ground and excited states when using CSMs [114]. Recent improvements to the Bethe-Salpeter kernel have made it possible for practitioners of CSMs to reproduce the empirical results. The new feature of modern Bethe-Salpeter kernel is the inclusion of a term closely related to the anomalous chromomagnetic moment, which reflects the influence of the EHM on the quark gluon vertex and which can be used to effectively describe the excited meson state very well.

In addition to studying mesons made up of light quarks, it is also worth exploring how the properties of mesons vary with meson mass. In the quark model view, if a valence light quark in pion is replaced by a strange quark, a kaon is formed. A kaon is also a Nambu–Goldstone boson in the chiral limit, however, in the real world, the strange quark, produced through the Higgs mechanism, is 27 times more massive than the current light quarks. Thus, the properties of the kaon are the result of the combined effect of the Higgs mechanism and the emergence of hadron mass. This has been revealed from the study of the parton distribution functions of kaons. The skewness of the distribution is caused by the heavier strange quark, while the overall broadening of the distribution is caused by the EHM. If mesons consisted of heavier quarks, charm, and bottom quarks, the Higgs mechanism would dominate and be the largest source of heavy meson properties. In particular, pseudoscalar mesons and heavy vector mesons are of particular interest as mesons with zero orbital angular momentum in the quark model [115,116]. Their distributions are usually narrower than those of light mesons, since it has been pointed out that the distribution in the heavy-quark limit is a Dirac delta function. The difference in distributions provides a clear picture of how the properties of mesons evolve with increasing meson mass, and the CSMs is a unified framework for describing all mesons, from pion to Upsilon.

It is worth mentioning that progress in mesons has also been extended to baryons. The properties of baryons are calculated using the Faddeev equation describing the three-quark scattering problem. Since the complete three-body problem in nature is much more complicated, the quark dynamical-diquark method is usually introduced, which is useful as a means of elucidating many qualitative features. Central to this approach is the incorporation of five different diquark correlations, of which the axial-vector diquark is of outstanding importance, to produce the correct baryon spectrum as well as baryon structure functions such as distribution functions, electromagnetic, axial, and pseudoscalar form factors.

In addition to the existing traditional hadrons, mesons, and baryons, many other new hadron states have been proposed experimentally and theoretically, such as exotic states, pentaquark, tetraquark, hybrid states, and glueballs. In the field of research on mesons consisting of heavy quarks, a comprehensive study of the charm family has been carried out thanks to a large amount of experimental data from the B-factory. As a result, states such as XYZ states, pentaquark, and tetraquark have extensively extended our knowledge of QCD bound states. In the field of research on mesons consisting of light quarks, there is a tendency to think that gluon degrees of freedom may also play a role in the formation of bound states, and thus there is speculation about the existence of states such as hybrid states and even glueballs [117]. This has been found from calculations of lattice QCD and CSMs, and future experiments, such as the 12 GeV upgrade experiment at Jefferson Lab, which will provide an opportunity to test these theoretical predictions.

Appendix A.3. Hadrons in Cold Dense Medium

In a cold and dense medium, i.e., for non-zero baryo-chemical potentials, quarks and emergent hadrons suffer the impact of the ambient matter. From low to high chemical potential domains, QCD will go through a phase of confinement and dynamical chiral symmetry breaking to a phase of deconfinement and chiral symmetry restoration. The key to the study is to determine the critical point/region at which the transition occurs and to which category the "phase transition" belongs.

Since the full domain of the finite chemical potential is currently not fully available in lattice QCD simulations, a complementary approach is CSMs [118–120], which expresses the dynamical chiral symmetry breaking and confinement in QCD, so that it can therefore be used as a tool to explore the properties of quark and hadron matter in cold dense medium, thus revealing relevant features of objects such as neutron stars. In the CSMs, the medium-induced dressed-quark propagator can be obtained by solving the quark gap equation in the medium, and the quark condensates are proportional to the matrix trace of the dressed quark propagator in the chiral limit. The quark condensate is crucial because it is commonly seen as the order parameter of the deconfinement (phase) transition. In some studies it has been shown that the chiral quark condensate is discontinuous with chemical potential, so that in the chiral limit the phase transition is of first order. Furthermore, it has been suggested that the QCD quark condensate may be completely contained in hadrons [121]. In addition to quarks, hadrons are also affected by the ambient medium at a non-zero chemical potential and, consequently, their masses change, showing noticeable deviations from the masses in vacuum. The appearance of a turning point in the chemical potential dependence of the hadron mass can also characterize the occurrence of chiral symmetry transition. It has also been proposed that increasing the chemical potential promotes the possibility of quark-quark Cooper pairing, i.e., diquark condensation. Quark-quark Cooper pairs are composite bosons with both electric and color charge, and thus superfluidity in quark matter entails superconductivity and color superconductivity.

These hadronic in-medium information is important not only for imaging the QCD phase diagram, but also for constructing a unified EoS from low-density nucleonic matter to high-density quark matter, and thus becomes crucial for determining the properties of neutron stars. Analog reasoning applies to other forms of strong-interaction matter which could govern new classes of compact stars, e.g., pion stars [1].

Appendix A.4. Supplementary Remarks

Before supplementing the above reflections by another approach to EHM w.r.t. condensates as fundamental QCD quantities, let us mention that the *ab initio* access to hadron vacuum masses is directly based on QCD as the theoretical basis of strong interaction. The current status is reviewed in Ref. [122]: a compelling description of the mass spectrum and various other hadron parameters is achieved by lattice QCD.

The operator product expansion relates parameters of a hadron model of the spectral function to a series of QCD condensates, most notably the above mentioned chiral quark condensate $\langle\bar{q}q\rangle$, the gluon condensate $\langle\frac{\alpha_s}{\pi}G^2\rangle$, the mixed quark-gluon condensate $\langle\bar{q}g_s\sigma Gq\rangle$, the triple gluon condensate $\langle g_s^3G^3\rangle$, the four-quark condensates $\langle\bar{q}\Gamma q\bar{q}\Gamma q\rangle$ (Γ denotes all possible structures formed by Dirac and Gell–Mann matrices) [123] and the poorly known condensates with higher mass-dimension. Further ingredients are the Wilson coefficients, which are accessible by perturbation theory [124]. In a strong-interaction medium, the condensates change: $\langle\cdots\rangle_0 \to \langle\cdots\rangle_{T,\mu_B}$; one could say that they are expelled from vacuum (label "0") by a higher spatial occupancy due to non-zero temperature and density (parametrized by μ_B) (similar to concerns as on the Higgs field condensate challenge such a picture of the vacuum, cf., [125] and follow-up citations). The induced dropping of condensates facilitates in-medium modifications of hadrons, in particular due the coupling to the chiral condensate, which is often considered as an order parameter of chiral symmetry. A recent review is Ref. [126].

In the baryon sector, the impact of the four-quark condensates and other in-medium-only condensates make unambiguous analyses of QCD sum rules somewhat vague. Previous factorizations relate the many four-quark condensates to the chiral condensate modulo some uncertain factor. For a comprehensive discussion, see Ref. [127], which focuses on the emergence of the nucleon mass, most notably m_p, from various quark and gluon condensates.

This brief journey should supplement our perspective of how the hadronic constituents of matter in compact stars acquire their masses and that the ambient medium modifies them. The very first step of gaining the above mentioned bare input masses by the Higgs mechanism is therefore left out, see Figure A1. The various bare quark masses appear in several QCD approaches as parameters adjusted to data. This is evidenced, e.g., in the approach [114]: A formula of two-quark meson masses is developed, $m(m_1, m_2)$, where $m_{1,2}$ refer to the bare quark masses. As shown in Figure 3 in Ref. [114], inspection of the contour lines $m(m_1, m_2) = const.$ can be used to pin down numerical values of bare masses $m_{1,2}$ which reproduce empirical values of ground states in the pseudo-scalar and vector channels including light u, d, strange and charm quarks at once; redundancy is used for cross checking. In addition, Regge trajectories become accessible to some extent [114,128].

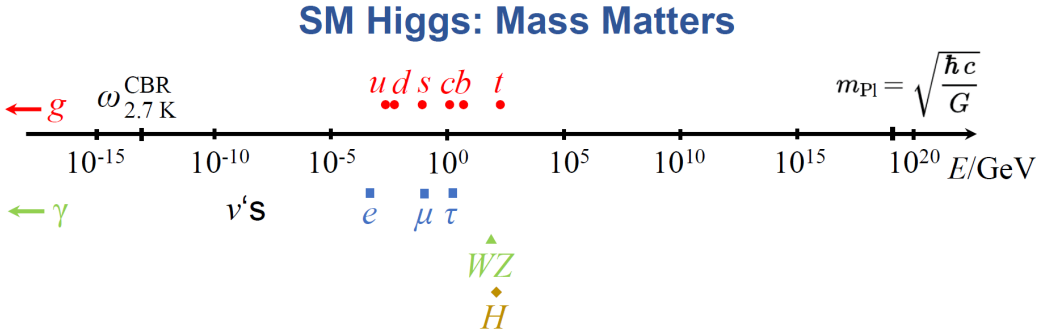

Figure A1. Masses within the SM. Mysterious concentration of bare SM masses (quarks $[u, d, s, c, t, b]$, leptons $[e, \mu, \tau]$, gauge bosons $[W^{\pm}, Z^0]$, Higgs $[H]$) and separation of neutrinos ($\nu's = [\nu_{e,\mu,\tau}]$) on a large energy scale ranging from present-day cosmic background radiation $\omega^{CBR}_{2.7\,K} \approx 0.233 \times 10^{-3}$ eV to Planck mass $m_{Pl} = \sqrt{\hbar c / G_N} \approx 1.22 \times 10^{19}$ GeV. Only the QED and QCD gauge Bosons $[\gamma, g]$ remain massless.

Appendix B. Holographic Approach to the EoS

Here we present a particular model of strong-interaction matter that is based on the famous AdS/CFT correspondence. In line with Refs. [129–131] we employ the action in a fiducial five-dimensional space-time with asymptotic AdS symmetry:

$$S_{EdM} = \frac{1}{2\kappa_5^2} \int \mathrm{d}^4x\, \mathrm{d}z\, \sqrt{-g_5} \left(R - \frac{1}{2} \partial^M \phi\, \partial_M \phi - V(\phi) - \frac{1}{4} \mathcal{G}(\phi) F_{\mathcal{B}}^2 \right), \tag{A1}$$

where R is the Einstein–Hilbert gravity part, $F_{\mathcal{B}}^{MN} = \partial^M \mathcal{B}^N - \partial^N \mathcal{B}^M$ stands for the field strength tensor of an Abelian gauge field $\mathcal{B}$ à la Maxwell with $\mathcal{B}_M \mathrm{d}x^M = \Phi(z)\, \mathrm{d}t$ defining the electro-static potential. An embedded black hole facilitates the description of a hot and dense medium, since the black hole has a Hawking surface temperature and sources an electric field, thus encoding holographically a temperature and a density of the system. Dynamical objects are a dilatonic (scalar) field ϕ and a Maxwell-type field Φ that are governed by a dilaton potential $V(\phi)$ and a dynamical coupling $\mathcal{G}(\phi)$ and geometry-related quantities. For a more general holographic approach to compact star physics, cf., Ref. [132]. Space-time is required to be described by the line element squared

$$\mathrm{d}s^2 = g_{MN} \mathrm{d}x^M \mathrm{d}x^N := \exp\{A(z, z_H)\} \left[f(z, z_H)\, \mathrm{d}t^2 - \mathrm{d}\vec{x}^2 - \frac{\mathrm{d}z^2}{f(z, z_H)} \right], \tag{A2}$$

where z_H is the horizon position, $z \in [z_H, \infty]$ is the radial coordinate, A is the warp factor, and f the blackness function.

The resulting Einstein equations are a set of coupled second-order ODEs to be solved with appropriate boundary conditions. The quantities V and $\mathcal{G}$ are tuned (in contrast to former work, we here put emphasis on side conditions which ensure that, at $\mu_B = 0$, no phase transition is facilitated outside the temperature range uncovered by the lattice data) to quantitatively describe the lattice QCD results [133]: Meanwhile, at $\mu_B = 0$, the datasets [134,135] are consistent, special combinations of quantities, e.g., e/p, enhance the small differences. This is, in particular, is striking at $T \in [130, 140]$ MeV, where a $+4\%$ (-10%) deviation in energy density (pressure) even changes the shape of the e/p curve when ignoring the error bars

$$\partial_\phi \ln V(\phi) = (p_1\phi + p_2\phi^2 + p_3\phi^3)\exp\{-\gamma\phi\}, \tag{A3}$$

$$\mathcal{G}(\phi) = \frac{1}{1+c_5}\left(\frac{1}{\cosh(c_1\phi + c_2\phi^2)} + \frac{c_3}{\cosh c_4\phi}\right) \tag{A4}$$

with parameters $\{p_{1,2,3}, \gamma\} = \{0.165919, 0.269459, -0.017133, 0.471384\}$ and $\{c_{1,2,3,4,5}\} = \{-0.276851, 0.394100, 0.651725, 101.6378, -0.939473\}$. These parameters and the scales implicitly refer to the QCD input, see Figure A2. The trace anomaly measure Δ, Equation (12), is exhibited in Figure A2, left, for various temperatures T and at baryon-chemical potential $\mu_B = 0$; the middle panel is for the ratio e/p. As argued in Ref. [105], the high-temperature, small-density and low-temperature, high-density behavior is strikingly different. A further crucial input quantity is the susceptibility $\chi_2 = \partial_{\mu_B} n_B|_{\mu_B=0}$, see the right panel in Figure A2. The length scale of the z coordinate is set by $L^{-1} = 1465$ MeV, which relates the horizon position z_H and temperature via $T = -1/(4\pi\partial_z f(z, z_H))|_{z=z_H}$, and by $\kappa_5^2 = 8.841$ fm^{-3}, which determines entropy density $s(T, \mu_B) = \frac{2\pi}{\kappa_5^2}\exp\{\frac{3}{2}A(z_H, z_H)\}$ and baryon density $n_B(T, \mu_B) = -\frac{\pi L^2}{\kappa_5^2}\partial_z^2\Phi(z, z_H)|_{z=0}$.

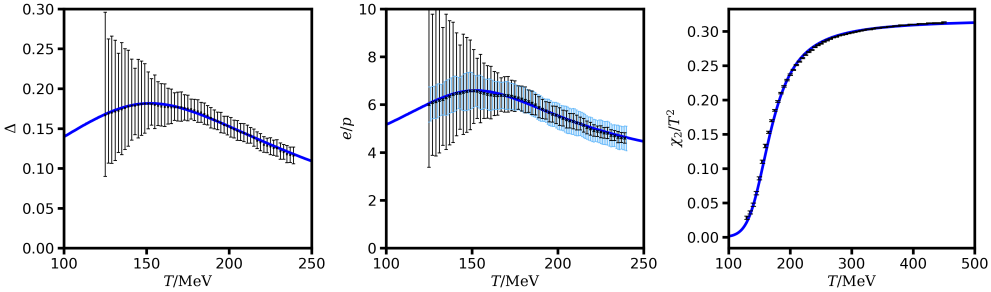

Figure A2. Trace anomaly measure Δ (**left** panel) and ratio e/p (**middle** panel) for the holographic model with tuned parameters to describe the lattice QCD data [133] (small crosses) at $\mu_B = 0$. Errors are constructed either from combining the respective maximum and minimum values (vertical error bars) or by error propagation in quadrature (blueish error bars). The scaled susceptibility χ_2/T^2 is displayed in the right panel; data (symbols) from [136].

The comparison of the scaled pressure p/T^4, ratio e/p, and scaled baryon density n_B/T^3 with the data [133] at $\mu_B/T = 1$ and 2 in Figure A3 exhibits good agreement in the small-μ_B region. That is, the model successfully maps QCD thermodynamics from the T axis into the T-μ_B plane, in particular towards the μ_B axis: $p(T) \mapsto p(\mu_B) = p(T(\mu_B))$. Curves of constant pressure, $T(\mu_B)|_{p=const}$, are determined by $dT/d\mu_B = -n_B(T, \mu_B)/s(T, \mu_B)$, (from $p(T(x), \mu_B(x)) = const$ and assuming a parametric representation $T(x)$ and $\mu_B(x)$ with x being the arc length. $\mathrm{d}p/\mathrm{d}x = (\partial p/\partial T)(\mathrm{d}T/\mathrm{d}x) + (\partial p/\partial\mu_B)(\mathrm{d}\mu_B/\mathrm{d}x) = 0$ then uses $s = \partial p/\partial T$ and $n_B = \partial p/\partial\mu_B$. The technicalities of holographically determining these quantities and the properties of the resulting EoS are relegated to a separate paper.) The left panel in Figure A4 is for a toy model demonstrating how the EoS given on the temperature axis is mapped to the chemical potential axis exhibited in Figure A4. The lattice data [133]

are for $T \in [125, 240]$ MeV at small values of μ_B (see the right panel). The "transport" into the restricted region of the T-μ_B plane by the holographic model is already an extrapolation, which requires a smooth pattern of $T(\mu_B)|_{p=const}$ curves without junctions, branchings, crossings, etc. The extrapolation of the data to $T < 125$ MeV and $T > 240$ MeV at $\mu_B = 0$ by the parameterizations (A3) and (A4) is another type of extrapolation. Thu,s the region beyond the displayed $p = const$ curves could be hampered by both types of uncertainties, but nevertheless may serve as educated guess of the cool EoS in the high-density realm. The benefit of such an approach is the direct coupling of the hot EoS, being an essential input in describing ultra-relativistic heavy-ion collisions by fluid dynamics, and the cool EoS, being the input for compact (neutron) star structure and (merger) dynamics.

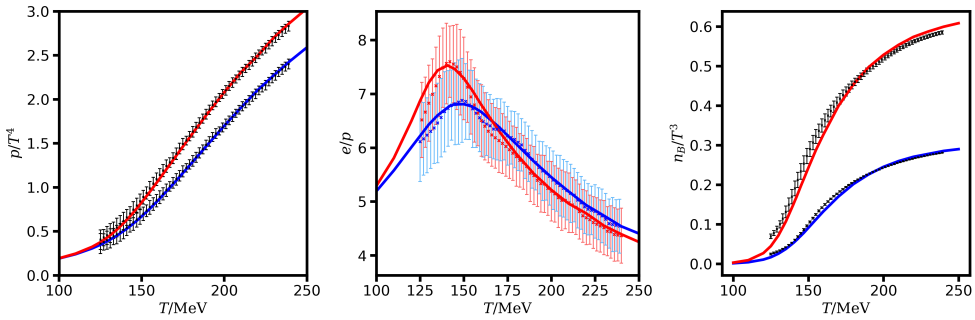

Figure A3. Scaled pressure p/T^4 (**left** panel), ratio e/p (**middle** panel), and scaled baryon density n_B/T^3 (**right** panel) as a function of temperature for $\mu_B/T = 1$ (blue) and 2 (red) in comparison with the data [133] (symbols with error bars).

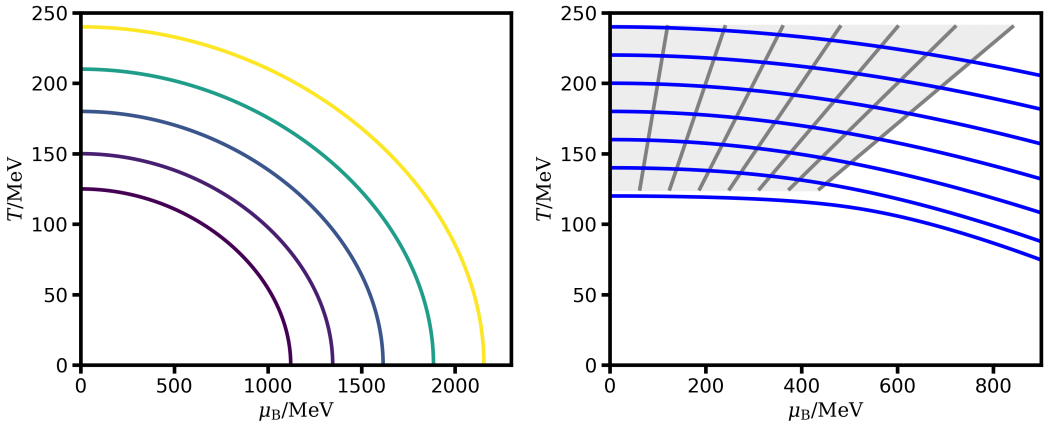

Figure A4. Curves of constant pressure over the T-μ_B plane. In such a way, the pressure data on the T axis are directly "transported" towards the μ_B axis, in particular $p(T = 0, \mu_B^{(0)}) = p_0 := p(T_0, \mu_B = 0)$ along the constant-pressure curve $T(\mu_B)|_{p=p_0}$ starting at $T(\mu_B = 0) = T_0$ and terminating at $T(\mu_B^{(0)}) = 0$. The energy density, with $s(T, \mu_B)$ and $n_B(T, \mu_B)$ given, then follows from $e = -p + Ts + \mu_B n_B$ (Gibbs–Duhem). **Left** panel: A simple toy model is employed here for the purpose of demonstration ($s = 4aT^3 + 2bT\mu_B^2$, $n_B = 4c\mu_B^3 + 2bT^2\mu_B$, and numerical values $b/a = 0.027384$, $c/a = 0.000154$ referring to a two-flavor ideal quark-gluon plasma). **Right** panel: For the holographic model (A1), (A3) and (A4) in a region (grey hatched) controlled by lattice QCD data [133] on the dark-grey beam sections.

Instead of explicitly using hadronic degrees of freedom to devise the holographic EoS, here the EoS as relation of energy density and pressure is solely deployed. Of course, the underlying hot QCD EoS is anchored in the common quark-gluon dynamics with intimate contact to the hadron observables.

References

1. Brandt, B.B.; Endrodi, G.; Fraga, E.S.; Hippert, M.; Schaffner-Bielich, J.; Schmalzbauer, S. New class of compact stars: Pion stars. *Phys. Rev. D* **2018**, *98*, 094510.
2. Roberts, C.D.; Richards, D.G.; Horn, T.; Chang, L. Insights into the emergence of mass from studies of pion and kaon structure. *Prog. Part. Nucl. Phys.* **2021**, *120*, 103883.
3. Roberts, C.D.; Schmidt, S.M. Reflections upon the emergence of hadronic mass. *Eur. Phys. J. ST* **2020**, *229*, 3319.
4. Tolos, L.; Fabbietti, L. Strangeness in Nuclei and Neutron Stars. *Prog. Part. Nucl. Phys.* **2020**, *112*, 103770.
5. Silva, H.O.; Holgado, A.M.; Cárdenas-Avendaño, A.; Yunes, N. Astrophysical and theoretical physics implications from multimessenger neutron star observations. *Phys. Rev. Lett.* **2021**, *126*, 181101.
6. Tews, I.; Pang, P.T.H.; Dietrich, T.; Coughlin, M.W.; Antier, S.; Bulla, M.; Heinzel, J.; Issa, L. On the Nature of GW190814 and Its Impact on the Understanding of Supranuclear Matter. *Astrophys. J. Lett.* **2021**, *908*, L1.
7. Tang, S.P.; Jiang, J.L.; Gao, W.H.; Fan, Y.Z.; Wei, D.M. Constraint on phase transition with the multimessenger data of neutron stars. *Phys. Rev. D* **2021**, *103*, 063026.
8. Margutti, R.; Chornock, R. First Multimessenger Observations of a Neutron Star Merger. *Ann. Rev. Astron. Astrophys.* **2021**, *59*, 155.
9. Nicholl, M.; Margalit, B.; Schmidt, P.; Smith, G.P.; Ridley, E.J.; Nuttall, J. Tight multimessenger constraints on the neutron star equation of state from GW170817 and a forward model for kilonova light-curve synthesis. *Mon. Not. Roy. Astron. Soc.* **2021**, *505*, 3016.
10. Yu, J.; Song, H.; Ai, S.; Gao, H.; Wang, F.; Wang, Y.; Lu, Y.; Fang, W.; Zhao, W. Multimessenger Detection Rates and Distributions of Binary Neutron Star Mergers and Their Cosmological Implications. *Astrophys. J.* **2021**, *916*, 54.
11. Annala, E.; Gorda, T.; Katerini, E.; Kurkela, A.; Nättilä, J.; Paschalidis, V.; Vuorinen, A. Multimessenger Constraints for Ultradense Matter. *Phys. Rev. X* **2022**, *12*, 011058.
12. Pang, P.T.H.; Tews, I.; Coughlin, M.W.; Bulla, M.; Broeck, C.V.D.; Dietrich, T. Nuclear Physics Multimessenger Astrophysics Constraints on the Neutron Star Equation of State: Adding NICER's PSR J0740+6620 Measurement. *Astrophys. J.* **2021**, *922*, 14.
13. Miller, M.C.; Lamb, F.K.; Dittmann, A.J.; Bogdanov, S.; Arzoumanian, Z.; Gendreau, K.C.; Guillot, S.; Ho, W.C.G.; Lattimer, J.M.; Loewenstein, M.; et al. The Radius of PSR J0740+6620 from NICER and XMM-Newton Data. *Astrophys. J. Lett.* **2021**, *918*, L28.
14. Miller, M.C.; Lamb, F.K.; Dittmann, A.J.; Bogdanov, S.; Arzoumanian, Z.; Gendreau, K.C.; Guillot, S.; Harding, A.K.; Ho, W.C.G.; Lattimer, J.M.; et al. PSR J0030+0451 Mass and Radius from *NICER* Data and Implications for the Properties of Neutron Star Matter. *Astrophys. J. Lett.* **2019**, *887*, L24.
15. Riley, T.E.; Watts, A.L.; Ray, P.S.; Bogdanov, S.; Guillot, S.; Morsink, S.M.; Bilous, A.V.; Arzoumanian, Z.; Choudhury, D.; Deneva, J.S.; et al. A NICER View of the Massive Pulsar PSR J0740+6620 Informed by Radio Timing and XMM-Newton Spectroscopy. *Astrophys. J. Lett.* **2021**, *918*, L27.
16. Riley, T.E.; Watts, A.L.; Bogdanov, S.; Ray, P.S.; Ludlam, R.M.; Guillot, S.; Arzoumanian, Z.; Baker, C.L.; Bilous, A.V.; Chakrabarty, D.; et al. A *NICER* View of PSR J0030+0451: Millisecond Pulsar Parameter Estimation. *Astrophys. J. Lett.* **2019**, *887*, L21.
17. Raaijmakers, G.; Greif, S.K.; Hebeler, K.; Hinderer, T.; Nissanke, S.; Schwenk, A.; Riley, T.E.; Watts, A.L.; Lattimer, J.M.; Ho, W.C.G. Constraints on the Dense Matter Equation of State and Neutron Star Properties from NICER's Mass–Radius Estimate of PSR J0740+6620 and Multimessenger Observations. *Astrophys. J. Lett.* **2021**, *918*, L29.
18. Pereira, J.P.; Bejger, M.; Tonetto, L.; Lugones, G.; Haensel, P.; Zdunik, J.L.; Sieniawska, M. Probing elastic quark phases in hybrid stars with radius measurements. *Astrophys. J.* **2021**, *910*, 145.
19. Christian, J.E.; Schaffner-Bielich, J. Twin Stars and the Stiffness of the Nuclear Equation of State: Ruling Out Strong Phase Transitions below $1.7n_0$ with the New NICER Radius Measurements. *Astrophys. J. Lett.* **2020**, *894*, L8.
20. Chatziioannou, K. Neutron star tidal deformability and equation of state constraints. *Gen. Rel. Grav.* **2020**, *52*, 109.
21. Motta, T.F.; Thomas, A.W. The role of baryon structure in neutron stars. *Mod. Phys. Lett. A* **2022**, *37*, 2230001.
22. Jokela, N.; Järvinen, M.; Remes, J. Holographic QCD in the NICER era. *Phys. Rev. D* **2022**, *105*, 086005.
23. Kovensky, N.; Poole, A.; Schmitt, A.. Building a realistic neutron star from holography. *Phys. Rev. D* **2022**, *105*, 034022.
24. Zhang, N.B.; Li, B.A. Impact of NICER's Radius Measurement of PSR J0740+6620 on Nuclear Symmetry Energy at Suprasaturation Densities. *Astrophys. J.* **2021**, *921*, 111.
25. Christian, J.E.; Schaffner-Bielich, J. Supermassive Neutron Stars Rule Out Twin Stars. *Phys. Rev. D* **2021**, *103*, 063042.
26. Gerlach, U.H. Equation of State at Supranuclear Densities and the Existence of a Third Family of Superdense Stars. *Phys. Rev.* **1968**, *172*, 1325.
27. Kämpfer, B. On the Possibility of Stable Quark and Pion Condensed Stars. *J. Phys. A* **1981**, *14*, L471.
28. Kämpfer, B. On stabilizing effects of relativity in cold spheric stars with a phase transition in the interior. *Phys. Lett. B* **1981**, *101*, 366.
29. Zdunik, J.L.; Haensel, P.; Schaeffer, R. Phase transitons in stellar cores, II Equilibrium configurations in general relativity. *Astron. Astrophys.* **1987**, *172*, 95.
30. Zdunik, J.L.; Haensel, P.; Schaeffer, R. Phase transitons in stellar cores, I Equilibrium configurations. *Astron. Astrophys.* **1983**, *126*, 121.
31. Li, J.J.; Sedrakian, A.; Alford, M. Relativistic hybrid stars with sequential first-order phase transitions and heavy-baryon envelopes. *Phys. Rev. D* **2020**, *101*, 063022.

32. Alford, M.G.; Sedrakian, A. Compact stars with sequential QCD phase transitions. *Phys. Rev. Lett.* **2017**, *119*, 161104.
33. Malfatti, G.; Orsaria, M.G.; Ranea-Sandoval, I.F.; Contrera, G.A.; Weber, F. Delta baryons and diquark formation in the cores of neutron stars. *Phys. Rev. D* **2020**, *102*, 063008.
34. Pereira, J.P.; Bejger, M.; Zdunik, J.L.; Haensel, P. Differentiating sharp phase transitions from mixed states in neutron stars. *arXiv* **2022**, arXiv:2201.01217.
35. Bejger, M.; Blaschke, D.; Haensel, P.; Zdunik, J.L.; Fortin, M. Consequences of a strong phase transition in the dense matter equation of state for the rotational evolution of neutron stars. *Astron. Astrophys.* **2017**, *600*, A39.
36. Li, J.J.; Sedrakian, A.; Alford, M. Relativistic hybrid stars in light of the NICER PSR J0740+6620 radius measurement. *Phys. Rev. D* **2021**, *104*, L121302.
37. Cierniak, M.; Blaschke, D. The special point on the hybrid star mass–radius diagram and its multi–messenger implications. *Eur. Phys. J. ST* **2020** *229*, 3663.
38. Ranea-Sandoval, I.F.; Han, S.; Orsaria, M.G.; Contrera, G.A.; Weber, F.; Alford, M.G. Constant-sound-speed parametrization for Nambu–Jona-Lasinio models of quark matter in hybrid stars. *Phys. Rev. C* **2016**, *93*, 045812.
39. Alford, M.G.; Han, S. Characteristics of hybrid compact stars with a sharp hadron-quark interface. *Eur. Phys. J. A* **2016**, *52*, 62.
40. Tan, H.; Dore, T.; Dexheimer, V.; Noronha-Hostler, J.; Yunes, N. Extreme matter meets extreme gravity: Ultraheavy neutron stars with phase transitions. *Phys. Rev. D* **2022**, *105*, 023018.
41. Glendenning, N.K.; Kettner, C. Nonidentical neutron star twins. *Astron. Astrophys.* **2000**, 353, L9.
42. Jakobus, P.; Motornenko, A.; Gomes, R.O.; Steinheimer, J.; Stoecker, H. The possibility of twin star solutions in a model based on lattice QCD thermodynamics. *Eur. Phys. J. C* **2021**, *81*, 41.
43. Alford, M.; Braby, M.; Paris, M.W.; Reddy, S. Hybrid stars that masquerade as neutron stars. *Astrophys. J.* **2005**, *629*, 969.
44. Klahn, T.; Blaschke, D.; Typel, S.; van Dalen, E.N.E.; Faessler, A.; Fuchs, C.; Gaitanos, T.; Grigorian, H.; Ho, A.; Kolomeitsev, E.E.; et al. Constraints on the high-density nuclear equation of state from the phenomenology of compact stars and heavy-ion collisions. *Phys. Rev. C* **2006**, *74*, 035802.
45. Most, E.R.; Motornenko, A.; Steinheimer, J.; Dexheimer, V.; Hanauske, M.; Rezzolla, L.; Stoecker, H. Probing neutron-star matter in the lab: Connecting binary mergers to heavy-ion collisions. *arXiv* **2022**, arXiv:2201.13150.
46. Adamczewski-Musch, J.; et al. [HADES], Probing dense baryon-rich matter with virtual photons. *Nature Phys.* **2019**, *15*, 1040.
47. Stephanov, M.A.; Rajagopal, K.; Shuryak, E.V. Event-by-event fluctuations in heavy ion collisions and the QCD critical point. *Phys. Rev. D* **1999**, *60*, 114028.
48. Karsch, F. Lattice QCD at high temperature and density. *Lect. Notes Phys.* **2002**, *583*, 209.
49. Fukushima, K.; Hatsuda, T. The phase diagram of dense QCD, *Rept. Prog. Phys.* **2011**, *74*, 014001.
50. Halasz, A.M.; Jackson, A.D.; Shrock, R.E.; Stephanov, M.A.; Verbaarschot, J.J.M. On the phase diagram of QCD. *Phys. Rev. D* **1998**, *58*, 096007.
51. Blacker, S.; Bastian, N.U.F.; Bauswein, A.; Blaschke, D.B.; Fischer, T.; Oertel, M.; Soultanis, T.; Typel, S. Constraining the onset density of the hadron-quark phase transition with gravitational-wave observations. *Phys. Rev. D* **2020**, *102*, 123023.
52. Blaschke, D.; Cierniak, M. Studying the onset of deconfinement with multi-messenger astronomy of neutron stars. *Astron. Nachr.* **2021**, *342*, 227.
53. Orsaria, M.G.; Malfatti, G.; Mariani, M.; Ranea-Sandoval, I.F.; García, F.; Spinella, W.M.; Contrera, G.A.; Lugones, G.; Weber, F. Phase transitions in neutron stars and their links to gravitational waves. *J. Phys. G* **2019**, *46*, 073002.
54. Cierniak, M.; Blaschke, D. Hybrid neutron stars in the mass-radius diagram. *Astron. Nachr.* **2021**, *342*, 819.
55. Kämpfer, B. Phase transitions in dense nuclear matter and explosive neutron star phenomena. *Phys. Lett. B* **1985**, *153*, 121.
56. Kämpfer, B. Phase transitions in nuclear matter and consequences for neutron stars. *J. Phys. G* **1983**, *9*, 1487.
57. Schertler, K.; Greiner, C.; Schaffner-Bielich, J.; Thoma, M.H. Quark phases in neutron stars and a 'third family' of compact stars as a signature for phase transitions. *Nucl. Phys. A* **2000**, *677*, 463.
58. Christian, J.E.; Zacchi, A.; Schaffner-Bielich, J. Classifications of Twin Star Solutions for a Constant Speed of Sound Parameterized Equation of State. *Eur. Phys. J. A* **2018**, *54*, 28.
59. Migdal, A.B.; Chernoutsan, A.I.; Mishustin, I.N. Pion condensation and dynamics of neutron stars. *Phys. Lett. B* **1979**, *83*, 158.
60. Kämpfer, B. On the collapse of neutron stars and stellar cores to pion-condensed stars. *Astrophys. Space Sci.* **1983**, *93*, 185.
61. Bertone, G.; Hooper, D.; Silk, J. Particle dark matter: Evidence, candidates and constraints. *Phys. Rept.* **2005**, *405*, 279.
62. Luzio, L.D.; Gavela, B.; Quilez, P.; Ringwald, A. Dark matter from an even lighter QCD axion: Trapped misalignment. *JCAP* **2021**, *10*, 001.
63. Hodges, H.M. Mirror baryons as the dark matter. *Phys. Rev. D* **1993**, *47*, 456.
64. Tulin, S.; Yu, H.B. Dark Matter Self-interactions and Small Scale Structure. *Phys. Rept.* **2018**, *730*, 1.
65. Karkevandi, D.R.; Shakeri, S.; Sagun, V.; Ivanytskyi, O. Bosonic dark matter in neutron stars and its effect on gravitational wave signal. *Phys. Rev. D* **2022**, *105*, 023001.
66. Dengler, Y.; Schaffner-Bielich, J.; Tolos, L. Second Love number of dark compact planets and neutron stars with dark matter. *Phys. Rev. D* **2022**, *105*, 043013.
67. Hippert, M.; Dillingham, E.; Tan, H.; Curtin, D.; Noronha-Hostler, J.; Yunes, N. Dark Matter or Regular Matter in Neutron Stars? How to tell the difference from the coalescence of compact objects. *arXiv* **2022**, [arXiv:2211.08590].

68. Beradze, R.; Gogberashvili, M.; Sakharov, A.S. Binary Neutron Star Mergers with Missing Electromagnetic Counterparts as Manifestations of Mirror World. *Phys. Lett. B* **2020**, *804*, 135402.
69. Alizzi, A.; Silagadze, Z.K. Dark photon portal into mirror world. *Mod. Phys. Lett. A* **2021**, *36*, 2150215.
70. Goldman, I.; Mohapatra, R.N.; Nussinov, S. Bounds on neutron-mirror neutron mixing from pulsar timing. *Phys. Rev. D* **2019**, *100*, 123021.
71. Berezhiani, Z. Antistars or antimatter cores in mirror neutron stars? *Universe* **2022**, *8*, 313.
72. Berezhiani, Z.; Biondi, R.; Mannarelli, M.; Tonelli, F. Neutron-mirror neutron mixing and neutron stars. *Eur. Phys. J. C* **2021**, *81*, 1036.
73. Beacham, J.; Burrage, C.; Curtin, D.; Roeck, A.D.; Evans, J.; Feng, J.L.; Gatto, C.; Gninenko, S.; Hartin, A.; Irastorza, I.; et al. Physics Beyond Colliders at CERN: Beyond the Standard Model Working Group Report. *J. Phys. G* **2020**, *47*, 010501.
74. Zöllner, R.; Kämpfer, B. Exotic Cores with and without Dark-Matter Admixtures in Compact Stars. *Astronomy* **2022**, *1*, 36.
75. Schaffner-Bielich, J. *Compact Star Physics*; Cambridge University Press: Cambridge UK, 2020.
76. Schulze, R.; Kämpfer, B. Cold quark stars from hot lattice QCD. *arXiv* **2009**, arXiv:0912.2827.
77. Baym, G.; Hatsuda, T.; Kojo, T.; Powell, P.D.; Song, Y.; Takatsuka, T. From hadrons to quarks in neutron stars: A review. *Rept. Prog. Phys.* **2018**, *81*, 056902.
78. Demorest, P.; Pennucci, T.; Ransom, S.; Roberts, M.; Hessels, J. Shapiro Delay Measurement of A Two Solar Mass Neutron Star. *Nature* **2010**, *467*, 1081.
79. Antoniadis, J.; Freire, P.C.C.; Wex, N.; Tauris, T.M.; Lynch, R.S.; van Kerkwijk, M.H.; Kramer, M.; Bassa, C.; Dhillon, V.S.; Driebe, T.; et al. A Massive Pulsar in a Compact Relativistic Binary. *Science* **2013**, *340*, 6131.
80. Fonseca, E.; Cromartie, H.T.; Pennucci, T.T.; Ray, P.S.; Kirichenko, A.Y.; Ransom, S.M.; Demorest, P.B.; Stairs, I.H.; Arzoumanian, Z.; Guillemot, L.; et al. Refined Mass and Geometric Measurements of the High-mass PSR J0740+6620. *Astrophys. J. Lett.* **2021**, *915*, L12.
81. Romani, R.W.; Kandel, D.; Filippenko, A.V.; Brink, T.G.; Zheng, W. PSR J0952−0607: The Fastest and Heaviest Known Galactic Neutron Star. *Astrophys. J. Lett.* **2022**, *934*, L18.
82. Abbott, R.; Abbott, T.D.; Abraham, S.; Acernese, F.; Ackley, K.; Adams, C.; Adhikari, R.X.; Adya, V.B.; Affeldt, C.; Agathos, M.; et al. GW190814: Gravitational Waves from the Coalescence of a 23 Solar Mass Black Hole with a 2.6 Solar Mass Compact Object. *Astrophys. J. Lett.* **2020**, *896*, L44.
83. Ecker, C.; Rezzolla, L. Impact of large-mass constraints on the properties of neutron stars. *arXiv* **2022**, arXiv:2209.08101.
84. Shao, Y. On the Neutron Star/Black Hole Mass Gap and Black Hole Searches. *Res. Astron. Astrophys.* **2022**, *22*, 122002.
85. Farah, A.M.; Fishbach, M.; Essick, R.; Holz, D.E.; Galaudage, S. Bridging the Gap: Categorizing Gravitational-wave Events at the Transition between Neutron Stars and Black Holes. *Astrophys. J.* **2022**, *931*, 108.
86. Reed, B.T.; Fattoyev, F.J.; Horowitz, C.J.; Piekarewicz, J. Implications of PREX-2 on the Equation of State of Neutron-Rich Matter. *Phys. Rev. Lett.* **2021**, *126*, 172503.
87. Annala, E.; Gorda, T.; Kurkela, A.; Nättilä, J.; Vuorinen, A. Evidence for quark-matter cores in massive neutron stars. *Nature Phys.* **2020**, *16*, 907.
88. Altiparmak, S.; Ecker, C.; Rezzolla, L. On the Sound Speed in Neutron Stars. *Astrophys. J. Lett.* **2022**, *939*, L34.
89. Ayriyan, A.; Blaschke, D.; Grunfeld, A.G.; Alvarez-Castillo, D.; Grigorian, H.; Abgaryan, V. Bayesian analysis of multimessenger M-R data with interpolated hybrid EoS. *Eur. Phys. J. A* **2021**, *57*, 318.
90. Oter, E.L.; Windisch, A.; Llanes-Estrada, F.J.; Alford, M. nEoS: Neutron Star Equation of State from hadron physics alone. *J. Phys. G* **2019**, *46*, 084001.
91. Lattimer, J.M.; Prakash, M. The Equation of State of Hot, Dense Matter and Neutron Stars. *Phys. Rept.* **2016**, *621*, 127.
92. Greif, S.K.; Hebeler, K.; Lattimer, J.M.; Pethick, C.J.; Schwenk, A. Equation of state constraints from nuclear physics, neutron star masses, and future moment of inertia measurements. *Astrophys. J.* **2020**, *901*, 155.
93. Anzuini, F.; Bell, N.F.; Busoni, G.; Motta, T.F.; Robles, S.; Thomas, A.W.; Virgato, M. Improved treatment of dark matter capture in neutron stars III: Nucleon and exotic targets. *JCAP* **2021**, *11*, 056.
94. Bell, N.F.; Busoni, G.; Robles, S. Capture of Leptophilic Dark Matter in Neutron Stars. *JCAP* **2019**, *06*, 054.
95. Das, H.C.; Kumar, A.; Kumar, B.; Patra, S.K. Dark Matter Effects on the Compact Star Properties. *Galaxies* **2022**, *10*, 14.
96. Das, H.C.; Kumar, A.; Patra, S.K. Dark matter admixed neutron star as a possible compact component in the GW190814 merger event. *Phys. Rev. D* **2021**, *104*, 063028.
97. Blaschke, D.; Ayriyan, A.; Alvarez-Castillo, D.E.; Grigorian, H. Was GW170817 a Canonical Neutron Star Merger? Bayesian Analysis with a Third Family of Compact Stars. *Universe* **2020**, *6*, 81.
98. Newton, W.G.; Balliet, L.; Budimir, S.; Crocombe, G.; Douglas, B.; Head, T.B.; Langford, Z.; Rivera, L.; Sanford, J. Ensembles of unified crust and core equations of state in a nuclear-multimessenger astrophysics environment. *Eur. Phys. J. A* **2022**, *58*, 69.
99. Huth, S.; Pang, P.T.H.; Tews, I.; Dietrich, T.; Fèvre, A.L.; Schwenk, A.; Trautmann, W.; Agarwal, K.; Bulla, M.; Coughlin, M.W.; et al. Constraining Neutron-Star Matter with Microscopic and Macroscopic Collisions. *Nature* **2022**, *606*, 276.
100. Raaijmakers, G.; Riley, T.E.; Watts, A.L.; Greif, S.K.; Morsink, S.M.; Hebeler, K.; Schwenk, A.; Hinderer, T.; Nissanke, S.; Guillot, S.; et al. A *NICER* view of PSR J0030+0451: Implications for the dense matter equation of state. *Astrophys. J. Lett.* **2019**, *887*, L22.

101. Raaijmakers, G.; Greif, S.K.; Riley, T.E.; Hinderer, T.; Hebeler, K.; Schwenk, A.; Watts, A.L.; Nissanke, S.; Guillot, S.; Lattimer, J.M.; et al. Constraining the dense matter equation of state with joint analysis of NICER and LIGO/Virgo measurements. *Astrophys. J. Lett.* **2020**, *893*, L21.
102. Gorda, T.; Komoltsev, O.; Kurkela, A. Ab-initio QCD calculations impact the inference of the neutron-star-matter equation of state. *arXiv* **2022**, arXiv:2204.11877.
103. Cassing, M.; Brisebois, A.; Azeem, M.; Schaffner-Bielich, J. Exotic Compact Objects with Two Dark Matter Fluids. *arXiv* **2022**, arXiv:2210.13697.
104. Kain, B. Dark matter admixed neutron stars. *Phys. Rev. D* **2021**, *103*, 043009.
105. Fujimoto, Y.; Fukushima, K.; McLerran, L.D.; Praszalowicz, M. Trace anomaly as signature of conformality in neutron stars. *Phys. Rev. Lett.* **2022**, *129*, 252702.
106. Marczenko, M.; McLerran, L.; Redlich, K.; Sasaki, C. Reaching percolation and conformal limits in neutron stars. *arXiv* **2022**, arXiv:2207.13059.
107. Hippert, M.; Fraga, E.S.; Noronha, J. Insights on the peak in the speed of sound of ultradense matter. *Phys. Rev. D* **2021**, *104*, 034011.
108. Marczenko, M.; Redlich, K.; Sasaki, C. Reconciling Multi-messenger Constraints with Chiral Symmetry Restoration. *arXiv* **2022**, arXiv:2208.03933.
109. Suleiman, L.; Fortin, M.; Zdunik, J.L.; Haensel, P. Influence of the crust on the neutron star macrophysical quantities and universal relations. *Phys. Rev. C* **2021**, *104*, 015801.
110. Gao, H.; Ai, S.K.; Cao, Z.J.; Zhang, B.; Zhu, Z.Y.; Li, A.; Zhang, N.B.; Bauswein, A. Relation between gravitational mass and baryonic mass for non-rotating and rapidly rotating neutron stars. *Front. Phys. (Beijing)* **2020**, *15*, 24603.
111. Ding, M.; Roberts, C.D.; Schmidt, S.M. Emergence of Hadron Mass and Structure. *Particles* **2023**, *6*, 57.
112. Dorkin, S.M.; Kaptari, L.P.; Hilger, T.; Kampfer, B. Analytical properties of the quark propagator from a truncated Dyson-Schwinger equation in complex Euclidean space. *Phys. Rev. C* **2014**, *89*, 034005.
113. Dorkin, S.M.; Kaptari, L.P.; Kämpfer, B. Accounting for the analytical properties of the quark propagator from the Dyson-Schwinger equation. *Phys. Rev. C* **2015**, *91*, 055201.
114. Greifenhagen, R.; Kämpfer, B.; Kaptari, L.P. Regge Trajectories of Radial Meson Excitations: Exploring the Dyson–Schwinger and Bethe–Salpeter Approach. In *Discoveries at the Frontiers of Science*; FIAS interdisciplinary science series; J. Fischer et al. Eds.; Springer Nature: Berlin/Heidelberg, Germany, 2020; p. 55.
115. Dorkin, S.M.; Hilger, T.; Kaptari, L.P.; Kampfer, B. Heavy pseudoscalar mesons in a Schwinger-Dyson–Bethe-Salpeter approach. *Few Body Syst.* **2011**, *49*, 247.
116. Dorkin, S.M.; Hilger, T.; Kampfer, B.; Kaptari, L.P. A Combined Solution of the Schwinger-Dyson and Bethe-Salpeter Equations for Mesons as $q\bar{q}$ Bound States. arx[b]:1012.5372nucl-th
117. Kaptari, L.P.; Kämpfer, B. Mass Spectrum of Pseudo-Scalar Glueballs from a Bethe–Salpeter Approach with the Rainbow–Ladder Truncation. *Few Body Syst.* **2020**, *61*, 28.
118. Maris, P.; Roberts, C.D.; Schmidt, S.M. Chemical potential dependence of pi and rho properties. *Phys. Rev. C* **1998**, 57, R28215,
119. Bender, A.; Poulis, G.I.; Roberts, C.D.; Schmidt, S.M.; Thomas, A.W. Deconfinement at finite chemical potential. *Phys. Lett. B* **1998**, *431*, 263.
120. Roberts, C.D.; Schmidt, S.M. Dyson-Schwinger equations: Density, temperature and continuum strong QCD. *Prog. Part. Nucl. Phys.* **2000** *45*, S1.
121. Brodsky, S.J.; Roberts, C.D.; Shrock, R.; Tandy, P.C. Confinement contains condensates. *Phys. Rev. C* **2012**, *85*, 065202.
122. Brambilla, N.; Eidelman, S.; Foka, P.; Gardner, S.; Kronfeld, A.S.; Alford, M.G.; Alkofer, R.; Butenschoen, M.; Cohen, T.D.; Erdmenger, J.; et al. QCD and Strongly Coupled Gauge Theories: Challenges and Perspectives. *Eur. Phys. J. C* **2014**, *74*, 2981.
123. Thomas, R.; Zschocke, S.; Kampfer, B. Evidence for in-medium changes of four-quark condensates. *Phys. Rev. Lett.* **2005**, *95*, 232301.
124. Buchheim, T.; Hilger, T.; Kampfer, B. Wilson coefficients and four-quark condensates in QCD sum rules for medium modifications of D mesons. *Phys. Rev. C* **2015**, *91*, 015205.
125. Brodsky, S.J.; Shrock, R. Condensates in Quantum Chromodynamics and the Cosmological Constant. *Proc. Nat. Acad. Sci. USA* **2011**, *108*, 45.
126. Gubler, P.; Satow, D. Recent Progress in QCD Condensate Evaluations and Sum Rules. *Prog. Part. Nucl. Phys.* **2019**, *106*, 1.
127. Thomas, R.; Hilger, T.; Kampfer, B. Four-quark condensates in nucleon QCD sum rules. *Nucl. Phys. A* **2007**, *795*, 19.
128. Fischer, C.S.; Kubrak, S.; Williams, R. Mass spectra and Regge trajectories of light mesons in the Bethe-Salpeter approach. *Eur. Phys. J. A* **2014**, *50*, 126.
129. DeWolfe, O.; Gubser, S.S.; Rosen, C. A holographic critical point. *Phys. Rev. D* **2011**, *83*, 086005.
130. Grefa, J.; Noronha, J.; Noronha-Hostler, J.; Portillo, I.; Ratti, C.; Rougemont, R. Hot and dense quark-gluon plasma thermodynamics from holographic black holes. *Phys. Rev. D* **2021**, *104*, 034002.
131. Critelli, R.; Noronha, J.; Noronha-Hostler, J.; Portillo, I.; Ratti, C.; Rougemont, R. Critical point in the phase diagram of primordial quark-gluon matter from black hole physics. *Phys. Rev. D* **2017**, *96*, 096026.
132. Järvinen, M. Holographic modeling of nuclear matter and neutron stars. *Eur. Phys. J. C* **2022**, *82*, 282.

133. Borsányi, S.; Fodor, Z.; Guenther, J.N.; Kara, R.; Katz, S.D.; Parotto, P.; Pásztor, A.; Ratti, C.; Szabó, K.K. Lattice QCD equation of state at finite chemical potential from an alternative expansion scheme. *Phys. Rev. Lett.* **2021**, *126*, 232001.
134. Borsanyi, S.; Fodor, Z.; Hoelbling, C.; Katz, S.D.; Krieg, S.; Szabo, K.K. Full result for the QCD equation of state with 2+1 flavors. *Phys. Lett. B* **2014**, *730*, 99.
135. Bazavov, A.; Bhattacharya, T.; DeTar, C.; Ding, H.T.; Gottlieb, S.; Gupta, R.; Hegde, P.; Heller, U.M.; Karsch, F.; Laermann, E.; et al. Equation of state in (2+1)-flavor QCD. *Phys. Rev. D* **2014**, *90*, 094503.
136. Bellwied, R.; Borsanyi, S.; Fodor, Z.; Katz, S.D.; Pasztor, A.; Ratti, C.; Szabo, K.K. Fluctuations and correlations in high temperature QCD. *Phys. Rev. D* **2015**, *92*, 114505.